

3. Automotive Metals - Cast

A. Improved Automotive Suspension Components Cast with B206 Alloy

Principal Investigator: Richard Osborne
Affiliation: General Motors Corporation
Address: 30001 Van Dyke Ave., Warren, MI 48090
(586) 575-7039; e-mail: richard.osborne@gm.com

Technical Project Administrator: Eric McCarty
Materials Technologies Consulting, LLC
Address: 5609 Hummingbird Lane, Clarkston, Michigan 48346
(248) 520-3009; e-mail: eric.mccarty@sbcglobal.net

Steve Logan, Materials Engineering
Chrysler LLC
800 Chrysler Drive, CIMS: 482-00-15
Auburn Hills, MI 48326
(248) 512-9485; e-mail: sl16@chrysler.com

Kasi Goundan, Materials Engineering
General Motors Corporation
Vehicle Engineering Center-VEC
Mail Code: 480-210-3B1
Warren, MI 48090-9020
(586) 575-2363; e-mail: kasi.k.goundan@gm.com

Jake Zindel, Technical Expert
Ford Motor Company
Mail Drop 3182 RIC, P.O. Box 2053
Dearborn, MI 48121
(313) 845-8559; e-mail: jzindel@ford.com

Technology Area Development Manager: William Joost
(202) 287-6020; e-mail: william.joost@ee.doe.gov

Field Project Officer: Magda A. Rivera
(304) 285-1359; email: magda.rivera@netl.doe.gov

Contractor: U.S. Automotive Materials Partnership
Contract No.: FC26-02OR22910

Objective

The objective of this program is to establish the commercial viability of B206 alloy for suspension components by providing needed fundamental information on this alloy system; and by overcoming technical issues, such as hot tearing and stress corrosion cracking, that limit the light weighting applications of this alloy. The B206 alloy has the potential to provide near net-shaped castings with mechanical properties equivalent to forged aluminum suspension components and ferritic ductile iron.

Approach

Four major technical focus points have been identified for this project. Accordingly, the work will be conducted in four separate phases:

Phase 1: Determine the effect of alloy composition on mechanical properties in the T4 and T7 heat treated conditions; and establish the feasibility of using less expensive versions of the alloy.

Phase 2: Study heat treatment of B206 alloy, and establish combinations of solution and aging time and temperatures which produce desirable strength with stress corrosion immunity. This portion of work will also determine the feasibility of using improved T7 heat treatment cycles, to increase elongation in this temper.

Phase 3: Create cost models for automotive suspension components produced by different processes and different materials.

Phase 4: Produce control arm castings using two different casting processes. Test components produced in the T4 and T7 tempers, to provide required CAE and design information, and establish the feasibility of using cast B206 alloy components to replaced forged aluminum parts.

Milestones, Metrics, and Accomplishments

PHASE 1: Complete

- The following Phase 1 studies were completed.
- The effect of chemistry and heat treatment on mechanical properties.
- The effect of cooling rate on mechanical properties.
- Hot tearing study.

The following are Phase 1 accomplishments.

- Optimized B206 T4 and T7 chemistries.
- A set of casting guidelines has been prepared for foundrymen who want to pour B206 alloy.

PHASE 2: Complete

The stress corrosion cracking study was completed.

PHASE 3: Complete

The cost model is complete. A Microsoft Excel spreadsheet was developed which can be used to compare costs of producing castings using A356-T6, B206-T4 and B206-T7 alloys.

PHASE 4: In progress

- The first and second casting trials at NEMAK using precision sand and semi-permanent mold respectively showed that the ability to achieve the mechanical properties equivalent to forged aluminum was highly dependent upon cooling rate.
- The third casting trial at Morel Industries using semi-permanent mold is still being tested.
- The fourth casting trial at Alotech using the Ablation casting process is still in process.

Future Direction

- Complete Phase 4 component testing.
- A full project report will be available in March, 2010.

Introduction

Aluminum B206 Cast Component Rationale

The 206 alloy is significantly stronger than the 356 alloy and has mechanical properties approaching some grades of ductile iron. It also has excellent high temperature tensile and low cycle fatigue strength. Consequently, this material could be used in a number of applications to reduce vehicle weight. Cost savings may also result, because less material would be required to provide the strength needed for the application. In spite of its excellent properties, however, the 206 alloy is seldom used because of its propensity for hot cracking. GKS Engineering has discovered a better method to grain refine this alloy, which reduces the tendency for hot cracking. This material has a number of potential applications, but its high strength and excellent ductility make it an ideal candidate for suspension components. Consequently, in the first stage of work (Project AMD 305 -- completed in May, 2002) control arms were produced via a tilt-pour/permanent mold casting process to establish the viability of this material for these safety critical components.

The work completed under AMD 305 showed that the B206 alloy could achieve mechanical properties equivalent to forged aluminum components and superior to that of typical automotive aluminum alloys. The tensile properties of permanent mold B206 alloy control arms were nearly the same as (or slightly better than) those found with many forged aluminum components, and the low cycle fatigue life of B206 alloy is ten times that of A356 alloy castings for an equivalent stress level. AMD 305 also showed that the permanent mold casting process, although suitable, may not be the best manufacturing process for the B206 alloy. Traditional sand casting and composite casting methods (such as Nematik's semi-permanent mold precision sand casting process) are more forgiving of hot cracking. The additional work proposed in this project will examine the technical feasibility of producing B206 alloy suspension components in other casting processes. Other important technical and commercial issues related to B206 will also be addressed. The objective is to provide the technical and economic data needed to justify commercial use of this material in suspension components.

Justification

Automakers are under increased pressure to reduce CO₂ emissions and improve fuel economy through increased CAFE standards. Because of their higher strength, B206 alloy structures have the potential to reduce vehicle mass, which is directly linked to improved CAFE and vehicle performance. There is also a potential for cost savings, because less material would be required when compared to conventional aluminum castings.

Phase 1: Complete

Determine the effect of alloy composition on mechanical properties in the T4 and T7 heat treated conditions; and establish the feasibility of using less expensive versions of the alloy.

Effect of Alloy Composition on Tensile Properties

A study of tensile properties versus alloy composition was first conducted by researchers at Alcan International using separately cast ASTM B108, permanent mold test bars. These results showed that best mechanical properties are obtained with two separate alloy compositions, depending on whether the T7 or the T4 temper is used. These two alloy compositions are:

1. T4 Temper - The alloy should contain 4.7 to 4.9% Cu, 0.35 % max. Mg and 0.2 % max. Mn. The expected tensile properties are 250-260 MPa yield strength, 430-450 MPa ultimate tensile strength, and 18-22% elongation. The maximum recommended copper in this alloy is 4.9%, since larger amounts may not go into solution during a standard heat treatment.
2. T7 Temper. - For a ductile T7 casting, the alloy should contain 4.2 to 4.4% Cu, 0.15% max. Mg, 0.2% max. Mn, <0.10%Fe, and <0.10%Si. The expected average tensile properties are 370-390 MPa yield strength, 445-455 MPa ultimate tensile strength, and 8 to 9% elongation.

Effect of Cooling Rate on Mechanical Properties

A second stage of phase one casting trials was also completed by NemaK researchers at their Central Development and Technology Center near Monterrey, Mexico. Twenty different alloy compositions were prepared and 'wedge' castings were made. The 'wedge' castings were poured to establish the tensile properties of the alloy as the solidification rate varied from 30 seconds to 30 minutes.

1. Zinc additions have no beneficial effect in this alloy. On the contrary, a small loss of strength was noted when significant amounts of zinc were present. For this reason, the recommended maximum limit of Zn in B206 alloy is 0.05%.
2. The best combination of mechanical properties was obtained when B206 alloy castings were heat treated to the T4 temper. In this condition the most rapidly solidified sections of the casting had 15-21 percent elongation, yield strength of 220-280 MPa, and an ultimate tensile strength of 370-450 MPa. The highest strengths were found at the higher range of alloy compositions.
3. Increasing the maximum limit of Mg from 0.35% to 0.55% would increase the yield strength of the B206 alloy in the T4 temper by 30 MPa.
4. The elongation and ultimate tensile strength of the material are sensitive to freezing rate. Rapid solidification is necessary for best properties. Data is presented on the amount of

porosity and undissolved copper-bearing phases in the material, as a function of freezing rate.

5. Castings heat treated to the T4 temper have a reasonable tolerance for the impurity elements Fe and Si. Depending on the desired elongation and the freezing rates in a casting, the maximum allowable limits for these elements can be increased. Accordingly, new composition limits were proposed for a “C” version of 206 alloy.
6. Metallographic examination of B206-T7 castings showed that a significant amount of Al-Cu-Mn-Fe phase precipitates at grain boundaries. It would be worth exploring different solution heat treatments, to see if it is possible to dissolve this phase. Alternatively, one might lower the Mn content in the alloy. It is possible that elongations in the T7 temper could be increased in this way.
7. Judging from the mechanical property data, it appears the Fe to Si ratio of the alloy may be important for B206-T7 castings. Further study would be required to establish if this is, in fact, the case.

Effect of chemistry on hot cracking

In addition to the cooling rate study, Nemak prepared hot crack test castings to determine the effect of alloy composition on castability. A number of important observations may be drawn from the Nemak study:

1. The hot crack resistance does not vary significantly over the composition range of the alloy.
2. The propensity for hot crack formation was much less in sand molds.

Design Guidelines

The Phase 1 studies were compiled into a set of casting and design guidelines for foundrymen who want to pour B206 alloy.

Phase 2: Complete

Study heat treatment of B206 alloy, and establish combinations of solution and aging time and temperatures which produce desirable strength with stress corrosion immunity. This portion of work will also determine the feasibility of using improved T7 heat treatment cycles, to increase elongation in this temper.

An extensive experimental program was undertaken at the University of Windsor in Ontario, Canada; with assistance from the laboratories of Alcan International. The program consisted of three primary tasks:

1. Effect of Aging on Mechanical Properties - The heat treatment of B206 alloy was studied in detail. The alloy conductivity, hardness and tensile properties were determined as a function of aging time and temperature. Limited studies were also performed on solution heat treatment, even though this work was not part of the original statement of work.
2. Measurement of Stress Corrosion - Measurements of the B206 alloy resistance to corrosion and stress corrosion cracking were made by two techniques. The first was the test for grain boundary attack outlined in ASTM G110. The second was the standard thirty day alternate immersion test as described in ASTM G44. There is a good correlation between the two

tests. However, the grain boundary attack procedure is not sufficiently accurate or reliable to replace the alternate immersion technique for qualification tests.

- Alternative T7 treatments - A number of alternative aging cycles were examined to improve the mechanical properties obtained for B206 alloy in the T7 temper. Two alternative heat treatments were identified as possible candidates, but the long aging times required make them cost prohibitive. Retrogression and reaging (RRA) techniques have been used successfully to improve mechanical properties in overaged (T7) Al-Zn-Mg alloys. Unfortunately, the aging mechanisms in B206 alloy (Al-Cu-Mg alloy system) are sufficiently different so that RRA techniques do not work.

Phase 3: Complete

Create cost models for automotive suspension components produced by different processes and different materials.

Cost models are difficult to construct, since actual costs of piece parts are dependent on many factors, which can change with time. Similarly, differences in a product’s design can favor one process or material over another. Even the selection of suppliers can influence the pricing when the manufacturing process is the same. And finally, actual production costs are difficult to obtain, since most companies consider their internal cost structure to be proprietary.

In light of the above issues, and the limited resources available for this phase of AMD 405, a simplified approach was taken. The intention was to answer the most basic commercial question: “Can automobile suspension control arms made of cast B206 aluminum alloy be competitive in the market place?” To answer this question a cost model was constructed to compare the differences between material and casting costs for the two aluminum alloys B206 (in both the T4 and T7 tempers) and A356 (in the T6 temper). Since A356-T6 alloy control arms and knuckles are now being manufactured in reasonable quantities, the cost of these parts represent a ‘calibration point’ for the phase 3 cost model. The actual cost model is an EXCEL spreadsheet. An example calculation using the model is shown [Table 1](#).

Table 1. Cost Model

Cost Comparison			
206-T4, 206-T7 and 356-T6 Alloys			
	356-T6	206-T4	206-T7
Mat'l Cost \$/kg	2.00	2.20	2.20
Casting Weight, kg	4.89	4.57	3.9
Engr'd Scrap, kg	2.10	2.23	1.90
Melting & Handling, \$/kg	0.5	0.5	0.5
Amortized Equipment, \$/kg	0.00	0.00	0.00
Casting Oper. \$/casting	9.78	10.05	8.58
Production Scrap, M/S	1.15	1.17	1.17
Solution Heat Treat, \$/kg-hr	0.0110	0.0110	0.0110
Solution Heat Treat, hrs	6.00	10.00	10.00
Aging Heat Treat, \$/kg-hr	0.0044	0.0044	0.0044
Aging Heat Treat, hrs	8.00	0.00	4.00
Cost of Heat Treatment, \$/part	0.4949	0.5027	0.4976
Value of mass savings, \$/kg	0.00	0.00	0.00
Base Cost, \$/casting	15.6119	16.03865	13.72519
Difference		-0.42675	1.886711

This calculation was made for the GM control arm serving as the ‘mule’ casting in AMD 405. The material (alloy) cost was based on prevailing prices at the time (early 2006). The casting weight was estimated from load criteria supplied by GM and stress analyses conducted by Sync Optima

Design. Other cost factors were either estimated from data supplied by commercial foundries or represent standard operating practices. The last item, the value of mass savings, represents the cost saving associated with lighter weight of an automobile. Undoubtedly there is some saving, but it has been assigned the value of zero for this calculation.

For the example shown above the B206 alloy in the T7 temper has the potential for significant cost reductions compared to A356 alloy castings, even when the market price of the B206 alloy is 10% more and when both casting designs are fully mass optimized. The reason for the cost saving is that the higher yield strength allows for the use of significantly less material. For the assumptions shown in the model, the cost savings would be \$1.89 per casting when using the B206 alloy in the T7 temper. However the 206 alloy in the T4 temper shows a small cost disadvantage of \$0.43 per casting. This is because the yield strength of the B206-T4 material is less, and so the weight saving is smaller, and not large enough to offset higher unit costs compared to A356 alloy.

The boxes, which are not highlighted in the above Excel chart, represent data entries entered by the user. Thus, it will be easy to make additional calculations for other conditions, adding to the utility of the cost model.

It should be noted that the relative costs of B206 and A356 alloys might be more favorable in cases where a part is designed to meet specified fatigue strengths. For a given stress loading, the fatigue life of B206-T4 alloy is nearly ten times that of the same casting produced in A356 alloy. (See AMD 305 final report.)

Phase 4: In Process

Produce control arm castings using two different casting processes. Test components produced in the T4 and T7 tempers, to provide required CAE and design information, and establish the feasibility of using cast B206 alloy components to replaced forged aluminum parts.

In this phase of the program front lower control arms were to be manufactured for extensive component testing and evaluation. At this time, the only complete test results available are from the limited number of castings produced at Nemak and are discussed below.

Nemak Castings

The first castings were made in a bonded sand mold. There were quality problems with the castings produced this way. The surface quality was poor, since a mold/molten metal reaction occurred which produced gas. There was also a good deal of shrinkage in several areas of the casting. (Without a metal drag the solidification was not sufficiently directional.) The risers, located in the cope of the mold had to be enlarged. This did not remove the shrinkage until insulated riser sleeves were placed in the risers. Nemak experimented with several different mold coatings, and they changed the mix used for the sand binder. Finally a number of castings having reasonable soundness and good surface quality were produced. Some of these castings were then heat treated and samples were excised from the casting for tensile tests. The results of the tests showed that the strength and elongation were much lower than required.

At this time technical members of AMD 405 had a long discussion with Nemak engineers about the situation. It was decided that the low mechanical properties were probably caused by slow solidification, and the absence of a metal drag. Nemak quickly made aluminum drag, which was sufficient to produce another 17 castings. Thermocouples were also placed in the all-sand and metal-sand composite molds, to measure the difference in solidification times with the two designs. The metal drag resulted in a shorter solidification time, better feeding, an elimination of the metal/mold reaction, and significantly better mechanical properties. The results obtained with each of the mule castings are summarized in [Figure 1](#).

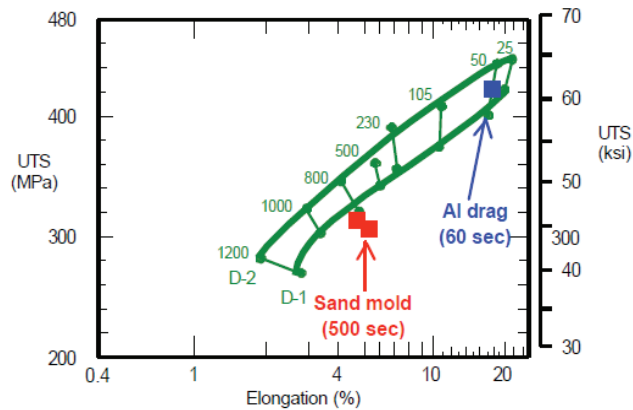


Figure 1. Tensile Properties of B206-T4 Alloy Castings

Alloy D-1 was very close to the composition used to produce Nemak FLCA castings. When an aluminum drag was employed the local solidification time was 60 seconds, and the tensile properties obtained (UTS = 412 MPa and 17.5% elongation) are indicated by the upper right box in Figure 1. It can be seen that the tensile properties obtained are almost exactly the same as found before in the ‘wedge’ casting for the same solidification rate.

When sand molds were employed the local solidification rate was 500 seconds. In these castings the mechanical properties were lower, as indicated by the two lower left boxes. For the sand mold castings the UTS and elongation were slightly lower than would be expected from the green curve, but the agreement is still reasonably good.

From these results it appears we may accurately predict mechanical properties in a commercial casting, at least for rapidly solidified parts. With the powerful computer simulation packages available today, one may easily determine freezing times at any point in a casting. Then, using the measured properties in the Nemak wedge casting (from the phase 1 casting trials in AMD 405), one can determine the corresponding tensile properties.

The most important observation resulting from the Nemak trials was that the mechanical properties of B206 alloy depend strongly on freezing rate in the casting. This observation was noted in the earlier, phase one casting trials at Nemak, where a ‘wedge’ casting was used.

Phase 4 Mule Castings

Currently, semi-permanent mold (sand cope/metal drag) and ablation mule castings, using the chemistries developed in Phase 1 and heat treated to the T4 and T7 tempers, are being tested at Westmoreland. Testing is expected to be complete in December, 2009.

Initial test results from Morel Industries suggested that the semi-permanent mold T7 castings would be the most promising castings to be bench tested and compared against forged aluminum control arms. Six of these control arms were machined and assembled by General Motors and are currently being bench tested. Bench testing is expected to be complete in December, 2009.

Conclusions

Conclusions are pending the results of Phase 4 casting trials.

Presentations/Publications/Patents

Below is a list of publications which, either in whole or in part, are based on results obtained from the two projects (AMD 305 and AMD 405) on B206 alloy.

1. G.K. Sigworth, F. DeHart and S. Millhollen: "Use of High Strength Aluminum Casting Alloys in Automotive Applications," pp. 313-322, Light Metals 2001 Métaux Léger, editors M. Sahoo and T.J. Lewis, Canadian Inst. Mining, Metallurgy and Petroleum, Montreal, Quebec, © 2001.
2. G.K. Sigworth and F. DeHart: "Recent Developments in the High Strength Aluminum-Copper Casting Alloy A206," AFS Transactions 2003, paper 03-135.
3. G.K. Sigworth, F. DeHart, J.F. Major and D. Donskoi: "Bulking Up Aluminum Alloys," Modern Casting, pp. 40-41, May, 2003.
4. G.K. Sigworth and J.F. Major: "Factors Influencing the Mechanical Properties of B206 Alloy Castings," Light Metals 2006, pp. 795-800 (2006).
5. J.F. Major and G.K. Sigworth: "Chemistry/Property Relationships in AA 206 Alloys," Trans. American Foundry Society, Vol. 114, pp. 117-128 (2006).
6. M. Manivannan, J.H. Sokolowski and D.O. Northwood: "Improving the Corrosion Resistance of a High Strength Al-Cu Alloy," paper presented at Corrosion and Prevention 2008, Nov. 16-19, 2008, Wellington, New Zealand.
7. Rodríguez, R. Chávez and J. Hernández, Y. Raymond and F. Major: "The Effect of Solidification Conditions and Alloy Composition on the Castability and Mechanical Properties of B206 Alloy," Trans. American Foundry Society, Vol. 117, pp. 79-92 (2009).
8. D. Jean and J.F. Major: "Chemistry/Property Relationships in AA 206 Alloys: Fatigue Behavior," Trans. American Foundry Society, Vol. 117, pp. 103-112 (2009).
9. D, Jean, J.F. Major, J.H. Sokolowski, B. Warnock and W. Kazprzak: Heat Treatment and Corrosion Resistance of B206 Aluminum Alloy," Trans. American Foundry Society, Vol. 117, pp. 113-120 (2009).

References

M.S. Misra and K.J. Oswalt: "Corrosion Behavior of Al-Cu-Ag (201) Alloy," Metals Engineering Quarterly, Vol. 16, pp. 39-44 (1976).

B.Magnesium Powertrain Cast Components

Principal Investigator: Bob R. Powell
General Motors Research & Development Center
30500 Mound Road, Mail Code 480-106-212
Warren, MI 48090-9055
(586) 986-1293; e-mail: bob.r.powell@gm.com

Technology Area Development Manager: William Joost
(202) 287-6020; e-mail: william.joost@ee.doe.gov

Contractor: United States Automotive Materials Partnership (USAMPI)
Contract No.: DE - FC26-02OR22910 through the DOE National Energy Technology Laboratory

Objective

Demonstrate and enhance the feasibility and benefits of using magnesium alloys in place of aluminum in structural powertrain components to achieve at least 15% mass reduction of the cast components.

Approach

- Identify, benchmark, and develop a design database of the potentially cost-effective, high-temperature magnesium alloys and, using this cast-specimen database, select the alloys that are most suitable for the magnesium components. (Task 1)
- Design, using finite-element analysis (FEA), an ultra-low-mass engine containing potentially four magnesium components (cylinder block, bedplate, structural oil pan, and front engine cover) using the most suitable low-cost, recyclable, creep- and corrosion-resistant magnesium alloys. (Task 2)
- Create a cost model to evaluate alloy, manufacturing, and technology costs to predict the cost-effective performance of the engine. (Task 2)
- During the execution of Tasks 1 and 2, identify and prioritize the critical gaps in the fundamental science of magnesium alloys and their processing that are barriers either to the progress of the project or to the use of magnesium in future powertrain applications. Seed-fund the most critical research, and promote additional identified needs to support further development of the magnesium scientific infrastructure in North America, thereby enabling more advanced powertrain applications of magnesium. This will be one aspect of the technology transfer deliverables of the Magnesium Powertrain Cast Components (MPCC) Project. (Task 3)
- Note that before addressing Tasks 4–6 and funding Task 3 research, an in-depth review of the engine design, including performance and durability predictions, alloy requirements and measured alloy properties, cost model, and predicted mass reduction will be conducted. Passing this gate review is necessary for entry into the second-half of the project, which has the goal of demonstrating/validating the engine design with respect to castability, manufacturability, performance, durability, and cost.
- Refine the engine component designs as necessary (updating to match the properties of the alloy selected for each component), design and build tools and patterns, and cast the engine components. (Task 4)

- Excise specimens from the cast components and develop a full mechanical and corrosion design database for the alloys. Create an original equipment manufacturer (OEM)—common material specification for magnesium powertrain alloys. (Task 5)
- Assemble complete engines, dynamometer-test the components, and conduct end-of-test teardowns. Refine the cost model to support determining the cost-effective performance of the engine. (Task 6)

Accomplishments

In the fiscal years (FYs) 2001 to 2008 Tasks 1 through 6 were completed.

- The final engine achieved a mass reduction for the magnesium components of 28 percent, nearly twice that of the original target.
- Cost analysis demonstrated that this mass reduction cost less than \$4 per pound; about twice the original target of less than \$2 per pound. Alloys were selected for each magnesium engine component, component designs were revised accordingly, casting tooling was designed and built and all four magnesium components were cast, machined, and delivered for component and engine testing. Component and engine testing were completed. The cylinder block passed thermal cycling and thermal soak testing; the head gasket passed pulsator testing; assembled engines with the full complement of magnesium components (block, oil pan and front engine cover) passed hot and cold scuff tests and a 672 hr coolant durability test; and an engine with magnesium oil pan and front engine cover passed a 675 hr high speed durability test. Finally, the five basic research projects in support of the objectives of Task 3 were completed.

The accomplishments in FY 2009 follow:

- FEA analysis was completed and the results confirmed the failure mechanism of the bulkheads during break-in operation of the engine for the Deep Thermal Shock Engine Test. The apparent cause of failure was little or no load transfer at the iron insert/magnesium interface due to the absence of a metallurgical bond between the insert and the magnesium. This problem can be overcome in future designs and is thus not a showstopper for the magnesium-intensive engine.
- Completed analysis of the coolant and teardown analysis of magnesium-intensive engine which was subjected to the 672 hr Coolant Corrosion Engine Test. The coolant protected the magnesium cylinder block very well and demonstrated that coolant corrosion is not a showstopper for the magnesium-intensive engine.
- Completed an NVH (noise, vibration, and harshness) assessment of the magnesium-intensive engine, the all aluminum baseline engine, and engines with one or more of the magnesium components. The results showed that magnesium and aluminum oil pans and front engine covers were indistinguishable from an NVH perspective. The magnesium cylinder block however, was about 2-6 dBA louder than the aluminum block, but most of the NVH increase was attributed to the deep skirt design of the magnesium block relative to the two piece aluminum block. These results also indicate that NVH is not a show stopper for a magnesium-intensive engine. Note: the NVH assessment was not part of the original project plan, but the remarkably quiet NVH of the magnesium-intensive engine during engine testing prompted support for this additional task.

Future Direction

Complete and distribute the final report for the Magnesium Powertrain Cast Components Project by March 31, 2010.

Introduction

The Magnesium Powertrain Cast Components (MPCC) project team's vision is of a magnesium-intensive engine that is cost-effective, light weight, and meets the manufacturability and durability requirements of the automotive industry. The approach taken was the redesign of an aluminum production engine (2.5L Ford Duratec) to a magnesium-intensive version; that is, to convert the cylinder block, bedplate, oil pan, and front engine cover to magnesium. All other parts of the engine were production carryover. The design, materials testing, tooling design and casting of the parts, and both component and assembled engine dynamometer testing were accomplished in prior years. Summaries can be found in previous progress reports. In 2009 we completed FEA of the bulkhead failures that were observed during break-in operation of one engine prior to deep thermal shock engine testing. We also completed analysis of the coolant and teardown analysis of magnesium-intensive engine that underwent 672 hr of coolant corrosion engine testing on an engine dynamometer. Incidentally, no bulkhead failures were observed in this test. Finally, the project team completed an additional set of tests to obtain a quantitative assessment of the noise, vibration and harshness (NVH) performance of the magnesium-intensive engine. These accomplishments complete the technical work of the Project. They are the subject of this, the FY 2009 Progress Report.

Deep Thermal Shock Test – Bulkhead Failure and Root Cause Analysis

The Deep Thermal Shock Test (DTS) was to have been the first of four durability tests for the magnesium-intensive engine. However, during break-in runs the behavior of the engine showed higher blow-by than the aluminum production engine and leakage past the crank seals and the oil fill cap. Subsequently, the engine oil pressure dropped and the engine began making bottom end noises. Inspection revealed complete failure of the two interior bulkheads and cracks propagated partially across bulkheads 1 and 4, see [Figure 1](#).

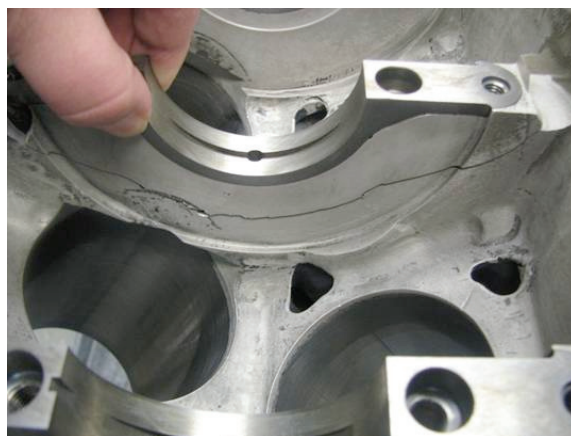


[Figure 1](#). Fracture of DTS engine bulkhead 3.

An intensive root cause analysis was launched by the MPCC project team. It included both teardown analysis of the engine and a re-evaluation of the FEA work done during Project Phase 1 engine design. The block alloy was AMT SC1. It was found that the composition was correct and that the microstructure was appropriately refined. Metal hardness values were also correct.

Examination of the bulkheads showed the absence of a metallurgical bond between the cast iron inserts and the magnesium bulkheads cast around them. A cross section of one of the bulkheads is shown in [Figure 2](#). The cast iron insert is shown in the middle of the figure, with magnesium on either side. Two areas of fracture surfaces were distinguished: fatigue and tensile overload. It was concluded that the tensile overload was the result of the absence of a bond between the inserts and the magnesium. Thus, being unable to transfer firing load to the inserts, the magnesium carried essentially the entire load and failed.



Figure 2. Sectioned bulkhead showing absence of interface bond between iron insert and magnesium bulkhead for DTS engine.

FEA used to design the magnesium block in Phase 1 of the Project did not predict the low safety factors (S.F.) that would have indicated risk of fatigue failure, see [Figure 3](#). The minimum S.F. was 2.65 at the outer edge of the M8 bolt hole. The reason for the good S.F. was due to the original assumption that there would be a good metallurgical bond. When the FEA was rerun with significantly reduced bond strength at the interface, the S.F. decreased to 1.48 at the same location and 1.26 in the treads, see [Figure 3](#). This was consistent with the metallurgical failure analysis.

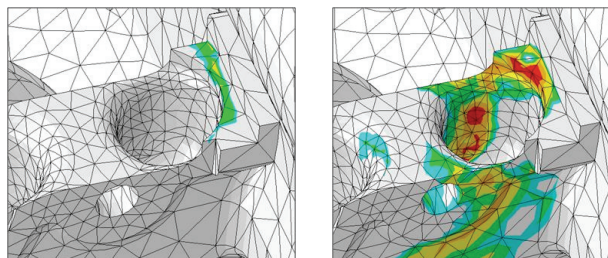


Figure 3. FEA safety factor (S.F.) predictions for bulkhead #1 in vicinity of M8 bolt hole: original FEA (left) and revised FEA (right) (see text).

The significance of this finding is that it shows how to avoid this failure in the future, namely by creating a strong bond between the insert and the magnesium. Because there are several ways to accomplish this, the failure of one magnesium-intensive engine of the four that were engine dynamometer tested, shows that this is not a technical showstopper for a magnesium-intensive engine.

672-hour Coolant Corrosion Test – Coolant Analysis and Engine Teardown Results

An important task of the Project was to determine the potential for protecting the magnesium block from corrosion by the engine coolant, specifically in the presence of ethylene glycol water-based coolant. Extensive bench testing was done of all considered magnesium alloys in

the earlier phase of the Project. After testing, the Honeywell experimental coolant was selected for the engine dynamometer coolant, see Figure 4.

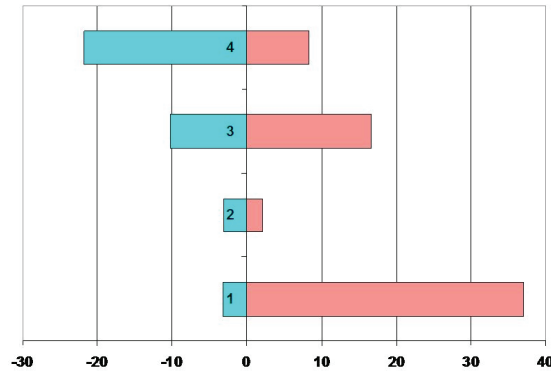


Figure 4. Weight loss of magnesium cylinder block alloy in D4340 (left) and D1384 (right) engine coolant tests. Honeywell coolant is #2.

Because the intended durability testing could not be done due to concerns about bulkhead failures (see above), the team chose to do a different durability test which was based on the Ford BL 102-02 standard for screening coolant behavior. This test simulates on-road engine cycles for a small vehicle. The major change to the test protocol was to run the engine at low load; low enough to protect the bulkheads, but high enough to achieve the necessary coolant temperatures to effectively test the coolant/component interfaces. The engine was run at 2000 rpm at 50 kN with periodic high and low temperature soaks. The test duration was forty-two days.

Testing went well and no issues were reported, including no indication of bulkhead failure as was reported during break-in for the DTS test (see above). Coolant samples were drawn before and after the test and at 96-hour intervals. The coolant samples were clear to visual inspection and free of sediment, see Figure 5.



Figure 5. Coolant specimens taken from the engine during coolant corrosion testing.

Analysis of the coolant showed negligible buildup of magnesium, iron, and zinc over the 672 hr of engine operation, see Figure 6. This was further evidence that the coolant formulation did protect the magnesium from corrosion.

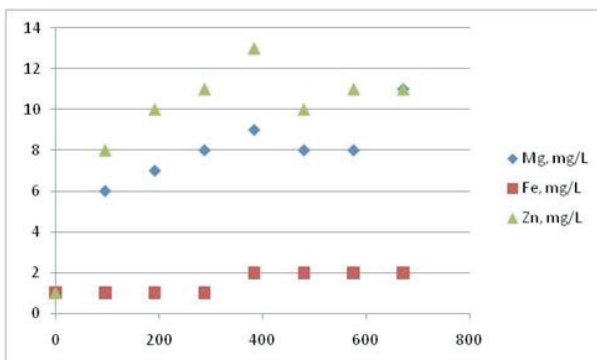


Figure 6. Mg, Fe, and Zn levels (mg/L) found in coolant specimens collected over the 672 hr engine test.

Visual inspection of the cylinder block and microscopic inspection of the internal coolant passages showed a slight discoloration of the metal surface, but otherwise minimal corrosion. These results indicate that corrosion of magnesium in engine coolant is not a showstopper for the magnesium-intensive engine.

NVH Assessment of the Magnesium-Intensive Engine

It is generally assumed that because of its lower density and stiffness, magnesium engine components will have worse NVH performance than aluminum and iron components. The MPCC project team originally intended a cursory NVH assessment of the magnesium-intensive engine, but when it was observed how relatively quiet the engines were, a new task was added to the Project: a quantitative assessment of the NVH performance of the MPCC engine, the original aluminum production engine and engines with sequential substitution of magnesium components for the original aluminum components. This assessment was completed in FY 2009. Six engines were prepared and tested in sequence in the test fixture.

Table 1. Hardware Configurations for NVH Testing

<i>Block</i>	<i>Oil Pan</i>	<i>Front Cover</i>
<i>Al</i>	<i>Al</i>	<i>Al</i>
<i>Al</i>	<i>Mg</i>	<i>Al</i>
<i>Al</i>	<i>Al</i>	<i>Mg</i>
<i>Al</i>	<i>Mg</i>	<i>Mg</i>
<i>Mg</i>	<i>Al</i>	<i>Al</i>
<i>Mg</i>	<i>Mg</i>	<i>Mg</i>

The baseline engine was the Jaguar 2.5L V6. Testing was done at the Roush NV Facility in Livonia, Mi. NVH measurements included: overall engine sound power; component sound power; and cold start noise. Five microphones were positioned around the engine at 1 meter distance from the engine. The exhaust and intake, as well as the bell housing, transmission, and drive shaft were acoustically wrapped and the engine was installed on rubber mounts, [Figure 7](#).



Figure 7. Set up for NVH assessment.

Overall Sound Power

With the magnesium block there was a significant increase in sound power, especially at high speed and load. The increase was 5-6 dBA in the 1250-1600 Hz range at 2500 rpm and 3-5 dBA in the 250-2500 Hz range at 4000 rpm, see also [Figure 8](#). In the opinion of the NVH engineers, the major reason for the NVH increase was the engine design rather than the material change.

The MPCC engine was a deep skirt design with unsupported crankcase walls. This weakened the bottom of the engine. As discussed in earlier progress reports, the change from a two-piece block (in aluminum) to a deep skirt was necessitated to address thermal expansion differences between magnesium and cast iron crank bore inserts.

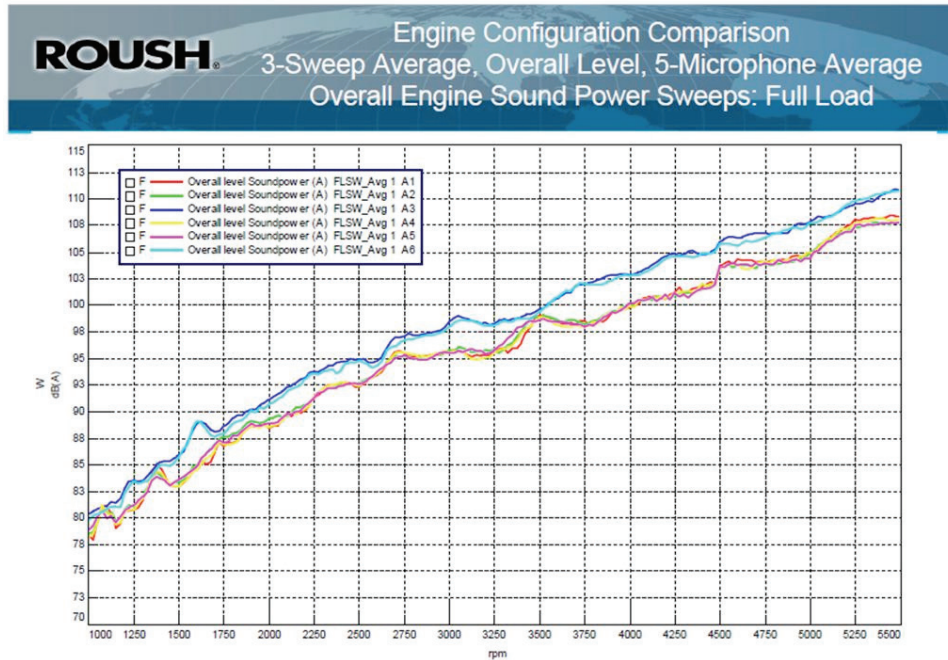


Figure 8. Overall engine power sweeps for Mg engine (upper curves) and Al engine (lower curves) with various Mg and Al oil pan and front engine cover combinations.

Component Sound Power

The effect of replacing the aluminum oil pan and front engine cover with magnesium either singly or jointly was also measured. The results shown in Figure 9 indicate that there was no significant noise increase when magnesium replaced aluminum. This is an important result; particularly with regard to the front engine cover which rather than being designed for greater stiffness, was actually designed for lower stiffness. As a fully compliant material, it did not contribute to noise radiation. Designing for greater compliance also enabled greater mass reduction through the use of thinner walls; 52% mass reduction from aluminum to magnesium.

RPM	Load	FEC Al/Al	FEC Mg/Al	SOP Al/Al	SOP Mg/Al	All Al	All Mg
Idle	None	81.5	82.8	76.6	76.6	73.6	74.6
2500	(81Nm)	96.0	96.4	90.6	91.8	89.3	92.7

Figure 9. Summary of component sound power for each engine configuration.

Cold Start Noise

Cold start testing was recommended to determine the effect of coefficient of thermal expansion (CTE) mismatch between the magnesium block (26×10^5 per degree C) and the aluminum piston (22×10^5 per degree C). Both the magnesium block and the aluminum block used aluminum pistons. At equal temperatures, the bore/piston clearance would be greater for the magnesium block than for the aluminum block.

The magnesium engine was subjectively louder at cold start and the sound quality was different as shown in Figure 10. Rattles and sound pressure impulses were detected. Piston slap was also heard occasionally with the magnesium engine, shown in Figure 11.

ROUSH Section 7: Medium Load Ramp-up, 20 to 80 Nm
Aluminum (A1) Engine vs Magnesium (A3) Engine
Right Microphone vs Engine rpm

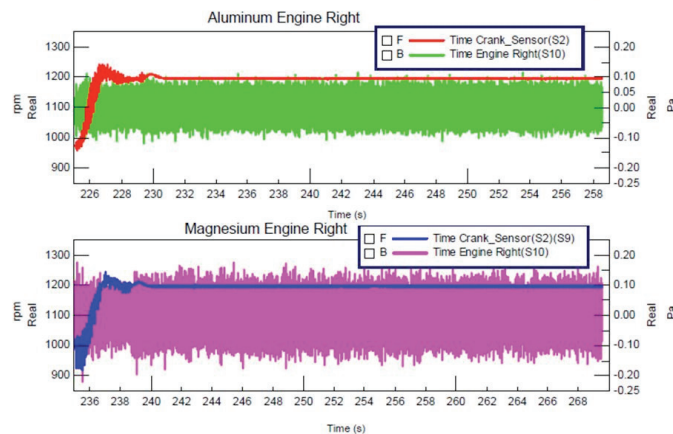


Figure 10. NVH performance at cold start of the aluminum block (upper) and the magnesium block (lower).

ROUSH Section 4: Ramp-down, Constant Load
Aluminum (A1) Engine vs Magnesium (A3) Engine
Right Microphone vs Engine rpm

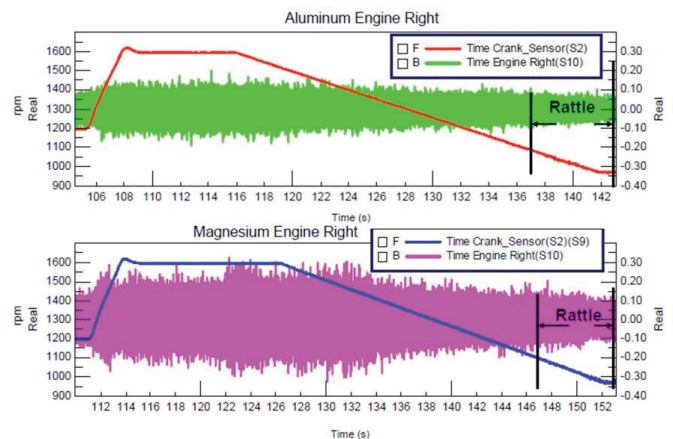


Figure 11. NVH performance at cold start of the aluminum block (upper) and the magnesium block (lower). Instances of piston slap are indicated.

In summary, the NVH performance of the magnesium engine was strikingly better than expected. With advanced design it is likely that the NVH difference could be made negligible.

Conclusions

In 2009 we were able to complete testing of both the major magnesium engine components and assembled engines. With the exception of the bulkhead failure in the DTS engine, all other engine tests were successful. Metallurgical analysis and FEA results confirm our hypothesis about the failure of the insert/magnesium interface. Thus, it appears that the thermal expansion mismatch problem can in fact be avoided through redesign.

Our results indicate that the anticipated technical issues for the magnesium-intensive engine (creep behavior and bolt load loss, corrosion, CTE mismatch, and NVH) do not appear to be “show stoppers” in the implementation of magnesium engine components. However, field performance and robustness have yet to be demonstrated.

Over the course of this project, our collaborations have yielded considerable valuable information about creep-resistant magnesium alloys, their castability, designing with them, and the cost factors entering into achieving cost-effective mass reduction.

Presentations/Publications/Patents

1. J.R. TerBush, A. Suzuki, N.D. Saddock, J.W. Jones, and T.M. Pollock, “Dislocation Substructures of Three Die-Cast Mg-Al-Ca-Based Alloys, *Scripta Materialia* **58** 914-917 (2008)
2. R.C. McCune, P.K. Mallick, and Z. Shi, “Study of Cathodic Metal Transfer to Magnesium Surfaces in Aqueous Environments and Engine Coolant Formulations by Surface Analytic Methods,” presented at the Magnesium Technology 2009 Symposium, TMS Annual Meeting, San Francisco, CA, February 19, 2009
3. J.R. TerBush, R. Adharapurapu, J.W. Jones, and T.M. Pollock, “Microsegregation and Creep in Mg-Al-Ca-Based Alloys,” presented at the Magnesium Technology 2009 Symposium, TMS Annual Meeting, San Francisco, CA, February 18, 2009
4. “Summary of the Tensile Properties of Creep-Resistant Magnesium Alloys,” to be published in the NADCA Product Specification Standards for Die Castings, the North American Die Casting Association, 2009
5. B.R. Powell, “Magnesium Powertrain Cast Components Project,” in DOE Semi-Annual Lightweighting Progress Report for Fiscal Year 2009
6. J.F. Quinn and B.R. Powell, “Magnesium Powertrain Cast Components Project,” presented at the 2009 US Department of Energy Merit Review, Washington, D.C. and posted on the DOE Vehicle Technologies Program website <http://annualmeritreview.energy.gov> on May 21, 2009

Acknowledgments

The success of this project is due to the dedicated efforts of a large number of team members at Ford, Chrysler, and General Motors. Particular thanks go to James Boileau (Ford), Bo Yang (Honeywell), and Clyde Bulloch (General Motors) for their work on bulk head failure analysis, coolant analysis, and NVH testing, respectively. The many other companies and organizations making up the project team are listed in Table 2. The continuing support of our respective companies and the US Department of Energy is gratefully acknowledged.

Endnote

¹Denotes project 304 of the Automotive Metals Division (AMD) of the United States Automotive Materials Partnership (USAMP), one of the formal consortia of the United States Council for Automotive Research (USCAR) set up by Chrysler, Ford, and General Motors (GM) to conduct joint, pre-competitive research and development.

Table 2. The MPCC Project Team

Core Team:	J. Allison, R. Beals, J. Hines, L. Kopka, R. McCune, W. Miller, L. Ouimet, B. Powell, J. Quinn, P. Ried
Product Design: - Alloy	Ford, GM, Chrysler, Magna Powertrain AMC, Dead Sea Magnesium, GM, Noranda, Norsk-Hydro, Solikamsk, VSMPO- Avisma
Casters:	Eck, Gibbs, Internet, Lunt, Meridian, Nemak, Spartan, Thixomat
Bore Treatment:	Gehring, Flame Spray
Tooling:	Becker, Delaware, EXCO, HE Vannatter
Coolants:	Ashland/Valvoline, ChevronTexaco, Honeywell/Prestone, CCI International
Fasteners:	RIBE
Friction Stir Welding:	Hitachi
Gaskets:	Dana/Victor Reinz
Testing Labs:	Amalgatech, CANMET, Stork, Westmoreland, Quasar
Prof. Organizations:	EKK, Flow Science, MAGMAsoft, Technalysis
Prof. Organizations:	IMA, NADCA
Project Administration:	Ried and Associates

C. High Integrity Magnesium Automotive Component (HIMAC)

Principal Investigator: Richard J. Osborne
General Motors Corporation
Mail Code 480-210-3B1
30001 Van Dyke Road
Warren, Michigan 48090-9020
Phone: (586) 575-7039; e-mail:richard.osborne@gm.com

Technology Area Development Manager: William Joost
(202) 587-6020; fax: (202) 586-2476; e-mail: william.joost@ee.doe.gov

Contractor: U.S Automotive Materials Partnership AMD 601
Contract No.: DE-FC26-02OR22910

Objective

- Develop and validate casting process technologies needed to manufacture Squeeze and Low-Pressure Permanent Mold (LPPM) cast magnesium automotive suspension components.
- Evaluate potential of emerging magnesium castings technologies, specifically the Ablation and T-Mag Processes
- Address critical technology barriers inhibiting magnesium application and component affordability
- Deliver magnesium control arm components from all processes for static and fatigue testing.

Approach

- Develop the metal casting process technologies necessary to cost-effectively manufacture high integrity (high ductility and strength, low porosity, free of objectionable oxides and inclusions) cast magnesium automotive chassis components using AM60 and AZ91 magnesium alloys.
- Develop existing aluminum Squeeze Casting and Low-Pressure Permanent Mold (LPPM) processes for the production of magnesium structural castings, and investigate two new emerging casting processes (Ablation and T-Mag).
- Develop enabling technologies and computer models critical to: increase cast magnesium automotive applications; predicting microstructure control, porosity: hot tearing and controlled mold filling.
- Investigate thermal treatments (now available for aluminum cast components) for the magnesium components cast from the chosen magnesium.
- By 2009, implement the findings for modeling; grain refinement; thermal treatment and cast magnesium control arm components (from all processes) in sufficient quantities from AZ91 and AM60 Mg alloys to prove the feasibility of each process that would be free of porosity and oxides and meet the X-ray ASTM Standards E-155 of level 2 or less.

Accomplishments

- Four selected aluminum casting processes (Squeeze Cast; LPPM; Ablation; T-Mag) have been developed for AM60 and AZ91 Mg alloys. Magnesium control arms have been successfully cast from all processes that meet the project's SOW requirements and X-ray ASTM E-155 Standards of level 2 or less.
- The electromagnetic pump (Task #6) was completed and installed in the LPPM machine (Figure 2) and calibration tests are currently being performed before castings are produced.
- Modeling techniques have been identified to minimize hot tear and porosity. The success of this model (Task #5) was proven when implemented in the Squeeze Cast process.
- Castings have been thermally treated with the advanced fluidized bed system, (Task #3) significantly reducing cycle time from a typical 8 hours to 2 hours (Figure 3).
- New R & D laboratory procedures were developed (and proved effective) for grain refinement (Task #4) using high-intensity ultrasonic vibration for improved dispersion of nanoparticles in molten alloy solidification behavior.
- The *Magnesium Vision 2020* Document (developed by the *Structural Cast Magnesium Development {SCMD} Project*) was used as references by the HIMAC Project Team as the new Mg casting processes were developed.
- Seven different Universities are actively involved in the HIMAC Project, including students from Undergraduate to PhD levels.
- Project cost expenditures match original budget numbers, and In-Kind support exceeds the projected forecast.

Future Direction:

- Representative sample castings will be selected from all processes and evaluations from each process will continue through CY 2010 using: X-ray inspection; static and fatigue testing for durability and mechanical properties will be compared to micro-porosity results.
- Cost studies will be completed that will compare the results of producing magnesium control arms from all processes identified in the HIMAC Project.
- The project team will continue to improve the potential weight savings/Mg control arm component versus steel stamping component, with process and tooling improvements.
- All data will be compiled and included in the HIMAC Final Report that will be distributed to all project participants at the closure of the project (CY2010)
- Several OEMs project team members expressed an interest in the further investigation of different high strength Mg alloys to improve mechanical properties of the Mg Control Arm. This investigation was not possible under the present HIMAC Project for many reasons, mostly financial limits. Also, this investigation was an item that was not part of the original Statement of Work (SOW). If this interest is further pursued, the best two (of the four HIMAC processes) will be chosen to do a new project (Phase 2) that will implement all of the findings and recommendations from the HIMAC project, but focusing on new high strength magnesium alloys. To implement such a project, an OEM customer will be required and the end results will be tested on a vehicle. Also, additional interest and support will be required by all OEMs that participate in the USAMP projects.

Introduction

The *High Integrity Magnesium Automotive Component (HIMAC-AMD 601) Project* addresses the near and mid-term metal casting development needs identified both in the project's original Statement of Work (SOW) and in the previously published *Magnesium Vision 2020* document that was included in the *Structural Cast Magnesium Development Project (SCMD AMD 111 & AMD 112)*. Understanding and eliminating the technical barriers that currently inhibit magnesium casting production will move the automotive industry into a better position to realize emerging automotive magnesium component needs, build needed magnesium industry infrastructure and develop tools that will be required to reduce the cost of magnesium components and enable sustainable production requirements.

To support the achievement of these processes, the project is divided into eight tasks. These tasks address key technology barriers that limit casting of magnesium automobile suspension, chassis applications and affect the manufacturing costs of these components as they are defined today:

- Task 1: Squeeze casting process development
- Task 2: Low pressure casting process development
- Task 3: Thermal treatment of castings including research into stepped heat treatment and fluidized beds.
- Task 4: Microstructure control during casting including grain refining and property improvement
- Task 5: Computer modeling and properties to enable prediction of casting quality and microstructure
- Task 6: Controlled Molten Metal Transfer and Filling
- Task 7: Emerging Casting Technologies
- Task 8: Technology Transfer

The project's goal was to investigate four (4) current aluminum casting processes (see [Figure 1](#)) that could be converted to magnesium, and produce the same magnesium component (front end control arm) from all four processes that would be: component tested (fatigue and static); X-rayed to meet SOW requirements of ASTM E-155 Standards (level 2 or less); evaluated for material and microstructure properties and provide cost information /casting/ process.



Squeeze Cast Process



Typical Mg Control Arm



LPPM Process



Ablation Process



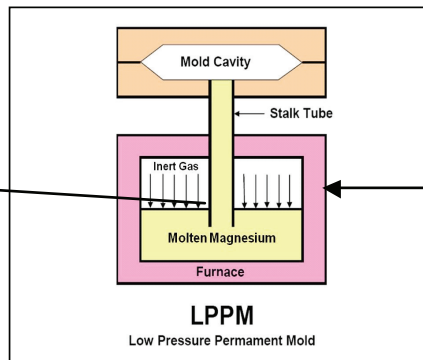
T-Mag Process

Figure 1. All Four types of Processes and the Mg Control Arm.

Further development of the LPPM system will continue through the end of the project, with the installation of the electromagnetic pump into the molten magnesium bath (as indicated below). The pump will quiescently deliver molten metal into the mold. This electromagnetic pump method has been used for the manufacture of aluminum components (blocks and heads for example), but has not been attempted with magnesium until the HIMAC Project was started. Additional magnesium control arms will be made by this revised process. The same evaluations that were previously mentioned will be completed and the results compared to all other castings produced by the four processes.



Typical LPPM System



Electromagnetic Pump

Figure 2. (Location of the electromagnetic pump into the LPPM System)

Thermal treatment of castings including research into stepped heat treatment and fluidized beds, as shown in Figure 3. A typical prototype production run (6/15/09) is shown in Figure 4, from the T-Mag Process. Castings were heat treated to both T-4 and T-6 processes and shipped to HIMAC facilities for further testing and evaluation.

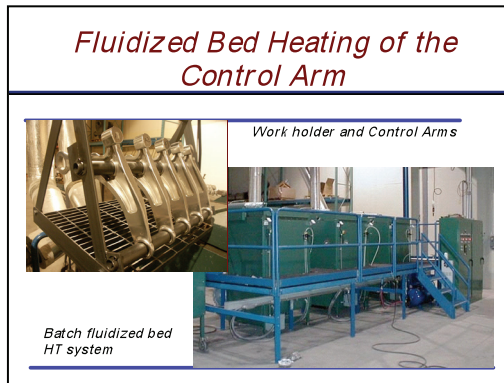


Figure 3. Batch Fluidized HT System



Figure 4. T-Mag Castings

Discussions:

The HIMAC project addresses many of the critical barriers (scientific and production implementation) to casting magnesium, as described in HIMAC Project's original SOW and detailed in the *Magnesium Vision 2020 Document* (sponsored by DOE under the SCMD Project).

Scientific investigations by HIMAC's academia support team have been instrumental in the investigation and defining requirements for the effective use of grain refinement; developing models for understanding porosity and hot tear conditions associated with different casting processes. These investigations will continue to the end of the project, and will provide new and critical support data from each process that will be useful to evaluate the components (and processes) in accordance with: X-ray; static and fatigue testing of the component; tensile and compression tests of samples (cut from the actual castings); microstructure evaluations for porosity and inclusions of all fractured surfaces, etc. All of this data will be evaluated at the end of the project, and correlated to each of the four processes.

Results:

The preliminary results (from all four processes) already indicate that magnesium casting components can be achieved from all four casting processes that heretofore were used only for casting aluminum components. This accomplishment is very significant, and in addition:

Grain Refinement (particle size, methods of application and related costs) have been identified for the two magnesium alloys used in the project. The use of nanoparticles in grain refinement and the methods of applications defined by the academia support team results in improved quality of the component and will reduce the excessive use of materials---thereby reducing costs. This accomplishment is also a significant achievement.

Preliminary results (X-ray and examination of fractured surfaces) already indicate castings can be provided with low porosity and will meet the SOW X-ray standards. Continued investigations through the end of the project will indicate the potential of each process to meet the SOW goals related to X-ray and porosity standards for the Mg alloys chosen.

Preliminary results from the new enabling technologies (Ablation and T-Mag processes) have indicated that these new processes can reduce process parameters to make high integrity magnesium components. Cost details/casting/process will be developed through the end of the report to identify the related costs of processing; facility costs, and enables the production of high integrity magnesium castings.

The use of controlled molten metal transfer and filling (electromagnetic pump) is currently being developed and evaluated. Results have already proven that this concept can pump molten magnesium, and castings will be provided and tested during CY2020. The use of this method of moving molten metal will eliminate many of the production and environmental issues associated with the standard cover gas over magnesium melts, and the ultimate result will yield higher quality castings.

All of the above results are from preliminary results of the investigations through CY 2009. Final results and specific details will be provided in the publication of the USAMP/DOE Final Report when the project ends in CY 2010. The Final Report (provided from the HIMAC Project) will be a major contributor to providing technical support in the understanding of magnesium components to the *Magnesium Front End Research and Development Project (AMD604)*.

Presentations/Publications/Patents

Pokorny, M.G. ; Monroe, C.A. ; and Beckermann,C. ; Prediction of Deformation and Hot Tear Formation Using a Viscoplastic Model with Damage, in Shape Casting : The 3rd International Symposium, eds.J Campbell, P.N. Crepeau and M. Tiryakioglu, TMS, Warrendale, PA, 2009, pp 265-272

Beckermann, C.; Prédiction of Porosity and Hot Tears in Magnesium Castings at Materials Science and Technology (MS&T) 2007 Conference, Detroit, MI September 2007.

Xue Y, Horstemeyer MF, McDowell DL, El Kadiri H, Fan J, Microstructure-based multistage fatigue modeling of cast AE44 magnesium alloys, Int J of Fatigue 2007 ; 29 : 666-76.

El Kadiri, Xue Y, Horstemeyer MF, Jordan B, and Wang P, Fatigue Crack Growth Mechanisms in a Die Cast AM50 Alloy, Acta Materialia 2006 ; 54 :5061-76.

Low Pressure Casting of Magnesium Alloys for Automotive Components; Greg Woycik, CMI Equipment & Engineering; American Foundry Society-111th Metalcasting Congress, May 15-18, 2007.

Magnesium Casting Technology Update; David Weiss, Eck Industries, Inc. ; American Foundry Society-111th Metalcasting Congress, May 15-18, 2007.

HIMAC; Magnesium Squeeze Casting Update ; Brian Szymanowski, Contech ; American Foundry Society-111th Metalcasting Congress, May 15-18, 2007.

High Integrity Magnesium Automotive Components (HIMAC) ; Bruce Cox, DaimlerChrysler NA, American Foundry Society-111th Metalcasting Congress, May 15-18, 2007.

Pokorny, M.; Monroe, C.; Beckermann, C.; Bichler, L.; and Ravindran, C.; "Prediction of Hot Tear Formation in a Magnesium Alloy Permanent Mold Casting," Int. J. Metalcasting, Vol. 2, No. 4, 2008, pp. 41-53

AFS 6th International Conference on Permanent Mold Casting of Aluminum and Magnesium—Feb, 11-12, 2008 Frisco TX.

Low Pressure Permanent Mold Casting of a Magnesium Lower Control Arm: G. G. Woycik, CMI Equipment and Engineering Inc., AuGres, MI; M. Marlatt, Marlatt Technologies, Three Lakes, WI (Publication and Presentation)

CastExpo '08—May 17, 2008, Atlanta GA.

Sponsored Research: Low Pressure Casting Process Simulation and Tooling Design for HIMAC's Magnesium Automotive Control Arm (08-148): Randy Sheng; Sarah Chen; Jagan Nath, General Aluminum, Madison Heights, MI; (Publication and Presentation).

Comparison of Gas Evolution Results from Chemically Bonded Cores In Contact with Magnesium and Aluminum Melts (08-048): Leonard Winardi; Preston Scarber; Robin Griffin, University of Alabama/Birmingham, Birmingham, AL; David Weiss, Eck Industries Inc., Manitowoc, WI; (Publication and Presentation).

Development of the Squeeze Cast Process for the USCAR HIMAC Project. (08-165): Richard Jacques, Contech US LLC, Portage, MI; John Jekl, Meridian Magnesium, Strathroy, ON, Canada: (2 Presentations)

Low Pressure Casting of a Magnesium Control Arm (08-166): Michael Marlatt, Marlatt Technologies, Three Lakes, WI; Gregory Woycik, Woycik Metallurgical Consulting LLC, Lapeer, MI; Chung-Whee Kim, EKK Inc., Farmington Hills, MI: (2 Presentations).

113 Metal-casting Congress: April 7-10, 2009; Paris Hotel; Las Vegas, Nevada

Panel 1: HIMAC Progress Review on Low Pressure and Squeeze Casting Processes (09-133):

1. Pressure Magnesium Casting of a Lower Control Arm: Michael Marlatt,
2. Marlatt Technologies; ATD Engineering & Machine LLC (Formerly CMI E & E).
3. HIMAC-Task #2 Support Low Pressure Simulation: Chung-Whee Kim, PhD., John D. Nitz, Ken Siersma-EKK, Inc.
4. Modeling of Mg Squeeze Casting Sponsored Research: Low Pressure Casting; Chung-Whee Kim, PhD., Ken Siersma-EKK, Inc.

Panel 2: Process Simulation of Advanced Casting Processes & Materials (09-149)

1. Process Optimization of High Integrity Magnesium Control Arm: Adi Sholapurwalla-ESI Group NA
2. Virtual Library of Cast Alloys: Jiten Shah-Product Development & Analysis (PDA) LLC.
3. Simulation of Core Gas Evolution: Andrei Starobin-Flow Science, Inc.

Panel 3: New Approaches to Magnesium Grain Refining (09-162)

1. New Approaches to Magnesium Grain Refining: Bruce Cox,-Alotech Ltd. LLC
2. Ultrasonic Grain Refining: Qingyou Han, PhD-Purdue University.
3. New Approaches to Magnesium Grain Refining: Mahi Sahoo PhD, Renata Zavadil, Lee Ann Sullivan-CANMET-MTL, Ottawa, Ontario, Canada; Xiaochun Li PhD, University of Wisconsin, Madison; Arun Gokhale-Georgia Tech, Atlanta Georgia.
4. Engineering an Efficient Grain Refiner for Magnesium Alloys: Partha Saha & S Srinath Viswanathan PhD-Department of Metallurgical & Materials Engineering; M. Shamsuzzoha PhD-Central Analytical Facility-University of Alabama.

Invited Conference Keynote Lecture

C. Beckermann, *Modeling of Deformation and Hot Tears*, at International Conference on Modeling of Casting, Welding, and advanced Solidification Processes X11, Vancouver, Canada, June 2009.

D. Casting/Solidification of Magnesium Alloys

Principal Investigator: Sergio D. Felicelli
Professor, Mechanical Engineering
Mississippi State University
210 Carpenter Engineering Bldg.
Mississippi State, MS 39762
(662)325-1201; e-mail: felicelli@me.msstate.edu

Co-Principal Investigator: Liang Wang
Research Assistant Professor
Center for Advanced Vehicular Systems, CAVS 2181
Mississippi State University, P.O. Box 5405
Mississippi State, MS 39762-5405
(662) 325-9235; home: (662) 325-5421; e-mail: liangw@cavs.msstate.edu

Co-Principal Investigator: John T. Berry
Professor, Mechanical Engineering
Mississippi State University
210 Carpenter Engineering Bldg.
Mississippi State, MS 39762
(662)325-7309; e-mail: berry@me.msstate.edu

Co-Principal Investigator: Adrian S. Sabau
Materials Processing Group
Materials Science & Technology Division
Oak Ridge National Laboratory
1 Bethel Valley Road, Oak Ridge, TN 37831-6083
(865) 241-5145; e-mail: sabaua@ornl.gov

Technology Area Development Manager: William Joost
(202) 287-6020; e-mail: william.joost@ee.doe.gov

Contractor: Mississippi State University
Contract No.: DE-AC05-00OR22725

Objective

Identify the root causes for porosity, segregation and other defects in magnesium cast parts and propose practical solutions for the improvement of casting processes.

Approach

Magnesium alloy cast parts are gaining increasing attention from the automotive sector, aiming at weight saving. However, the casting of magnesium alloys is still plagued with problems that are difficult to solve: porosity, macrosegregation, oxide entrainment, irregularity of microstructure, corrosion, machining safety, etc. This research project addresses the fundamental behavior of solidification phenomena that lead to undesired defects (e.g., porosity, macro-segregation, mushy zone) in magnesium cast parts, with the objective of developing new or improved casting methods for these alloys.

Accomplishments

Tasks

Added a new pore nucleation and growth model to our solidification simulator MULTIA, based on the alloy content of impurities or inclusions. Model was validated with A356 and AZ91.

Upgraded MULTIA with a new algorithm of interdendritic fluid flow based on the fractional step method. This upgrade allowed us to simulate dendritic solidification with convection in unstructured finite element meshes of triangles.

Determined unavailable physical properties of alloys AZ91 and AE42 through thermodynamic calculations with software packages ThermoCalc and JMatPro, which were needed for the solidification simulations.

Determined, numerically and experimentally, correlation porosity vs. cooling rate for alloy AZ91

Performed castings at ORNL under different cooling rates for alloys AZ91 and AE42

Performed microstructure analysis of AZ91 and AE42 samples via XRCT, SEM and optical microscopy to quantify fraction of porosity, dendrite arm spacing, and correlate with local cooling rate. FY09

Determined the presence of oxide films at pore surfaces of cast samples. FY09

Performed 4-point bending tests and analyzed fracture surfaces, exposing oxide defects. FY09

Developed dendrite growth model for AZ91 based on cellular automaton technique. First model to predict six-fold geometry of Mg dendrites. FY09

Publications

8 refereed journal articles and 5 refereed conference papers were produced by this research.

Students

3 Ph.D. students worked, directly or indirectly, in this project (one of them already graduated)

Competitive Proposals

Five competitive proposals (3 National Science Foundation, 1 National Aeronautics and Space Administration, and 1 Department of Defense) for a total of \$910,000 were awarded thanks in part to the seed stimulus provided by this earmark funding.

Introduction

Magnesium cast alloys, such as AZ91 and AE42, are gaining increasing attention in the struggle for weight saving in the automobile industry [1]. However, in many cases the consistent production of sound magnesium castings is marred by the stubborn persistence of some defects that are difficult to remove: porosity, macrosegregation, oxide entrainment, irregularity of microstructure, etc. The formation of microporosity in particular is known to be one of the primary detrimental factors controlling fatigue lifetime and total elongation in cast light alloy components.

Many efforts have been devoted to the modeling and experiments of porosity formation in the last 20 years. More recently, rather sophisticated models have been developed to include the effect of pores on fluid flow (three-phase transport) [2], multiscale frameworks that consider the impingement of pores on the microstructure [3], effects of finite-rate hydrogen diffusion in

the formation of pores [4]. A recent review on the subject of computer simulation of porosity and shrinkage related defects has been published by Stefanescu [5]. The new mechanisms of pore formation based on entrainment of oxide films during the filling of aluminum alloy castings have been identified and documented [6-11]. Oxide film defects are formed when the oxidized surface of the liquid metal is folded over onto itself and entrained into the bulk liquid. A layer of air is trapped between the internal surfaces of the oxide film, which leads to the porosity formation in the solidified castings. The entrainment process due to surface turbulence is usually rapid, in the order of milliseconds; therefore the time is very limited to form new oxide film on the fresh surface, so that the entrained oxide film can be very thin, in the order of nanometers [6].

Four parts are included in this work. 1) Gas porosity model in aluminum and magnesium alloys; 2) Porosity and oxide films in AZ91; 3) Porosity and oxide films in AE42; 4) Dendrite growth model in magnesium alloy solidification.

The results presented in this report are relevant to a gravity-pour casting process for which we develop a porosity model. This model is not applicable to HPDC process which involves flow conditions and time scale, vastly different from the one treated by the current solidification model. The role of oxide films in adding porosity formation could carry over to other LPPM and DC casting processes.

Gas porosity model in aluminum and magnesium alloy

A numerical model of hydrogen porosity formation during solidification was developed and applied to aluminum alloy A356 and magnesium alloy AZ91. The model (named MULTIA) solves the conservation equations of mass, momentum, energy, and each alloy component within a continuum framework in which the mushy zone is treated as a porous medium of variable permeability. In order to predict whether microporosity forms, the solidification shrinkage due to different phase densities, the concentration of gas-forming elements and their redistribution by transport during solidification were later added to the model. In this form, the model was able to predict regions of possible formation of porosity by comparing the Sievert's pressure with the local pressure, but it lacked the capability of calculating the amount of porosity. This model has already been presented in detail in Refs. [12] and [13].

Modeling results of the distribution of pore volume fraction and pore size in A356 are compared with published works. In view of the limited availability of experimental data for Mg-alloy gravity poured castings, the model is used to make a comparison study of porosity formation between aluminum alloy A356 and magnesium alloy AZ91, assuming similar casting conditions. The minimum initial hydrogen content that leads to the formation of gas porosity is compared for both alloys. The two parameters of the porosity model, initial pore size and concentration of inclusions, are taken from the A356 data. We acknowledge that these are rather arbitrary assumptions, but in view of the lack of more suitable data, our purpose is only to observe how porosity in AZ91 would form and evolve under these conditions and make a side to side comparison with A356.

Figure 1 shows the variation of pore volume fraction and pore diameter versus cooling rate in the solidified casting of A356 aluminum alloy for the initial hydrogen content of 0.11 cc/100g.

In Figure 1, the pink dots are calculated values that span throughout the casting; each dot represents the pore volume fraction or pore diameter calculated at a mesh node in the casting. A least squares fit of the calculated values is also shown as a solid black line. The experimental data of Fang and Granger [14] are indicated as green dots; these were taken by manual reading from their paper, so bars estimating possible reading error are added. The experimental green dots represent average values measured at a certain section of the casting, while the simulation

shows the space variation within the entire casting. Certainly, the pore volume fraction and diameter are affected by other solidification variables in addition to cooling rate, but an average trend can be identified which is that they both decrease for higher cooling rates. The quantitative agreement of simulated results with the experimental data is reasonable, considering that we are using a relatively simple two-dimensional continuum model.

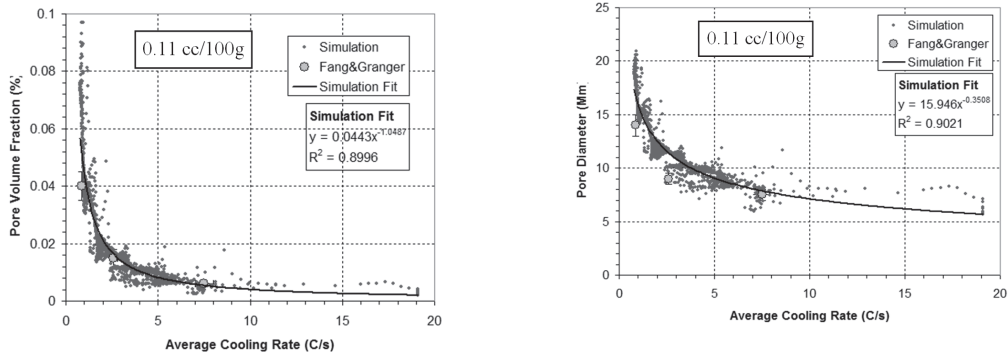


Figure 1. Pore volume fraction and pore diameter vs. cooling rate for A356 (H content: 0.11 cc/100g)

Figure 2 shows the variation of pore volume fraction and pore diameter vs. cooling rate in the solidified casting of AZ91 magnesium alloy for the initial hydrogen content of 17.72 cc/100g. Similarly as in Figure 1, the pink dots are calculated values that span all the casting; each dot represents the pore volume fraction or pore diameter calculated at a mesh node in the casting. A least squares fit of the calculated values is also shown as a solid black line. Both pore volume fraction and pore diameter show a similar trend between AZ91 and A356, suggesting that porosity develops similarly in both alloys. However, the minimum initial concentration of hydrogen to form pores in AZ91 is much higher than in A356. The high initial hydrogen content (~ 16 ppm) needed to form porosity in AZ91 is attributed to the high solubility of hydrogen in this alloy.

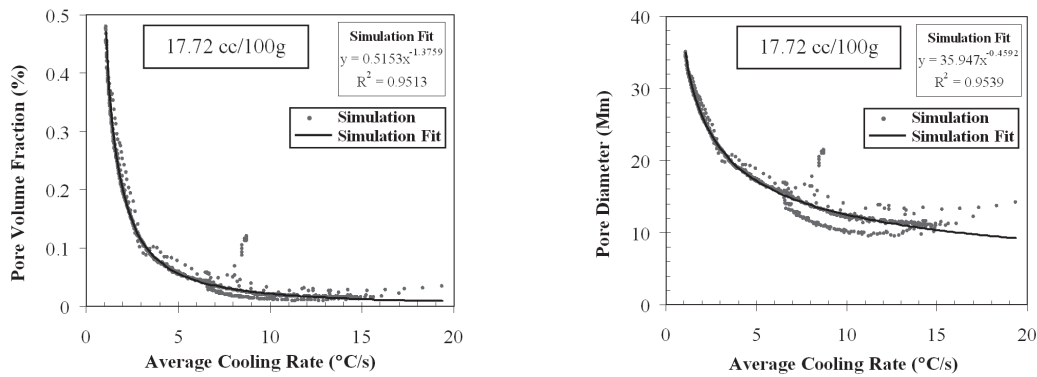


Figure 2. Pore volume fraction and pore diameter vs. cooling rate for AZ91 (H content: 17.72 cc/100g)

The porosity growth rate, R_p [$\mu\text{m}/(\text{cc}/100\text{g})$], due to the change of the initial hydrogen content in the liquid alloy is defined as

$$(1) \quad R_p = \frac{d_1^p - d_2^p}{C_1^H - C_2^H}$$

where d_1^p and d_2^p are the pore diameters at a certain cooling rate for different initial hydrogen content C_1^H and C_2^H , respectively. Figure 3 shows the porosity growth rate as a function of the average cooling rate when the initial hydrogen content increases in the amount of 0.14 cc/100g for A356 and AZ91 under the same casting conditions. It is observed that the porosity

growth rate for AZ91 is much smaller than for A356, which is expected because the diffusion coefficient of hydrogen in liquid magnesium is smaller than that in liquid aluminum, as shown in Figure 4.

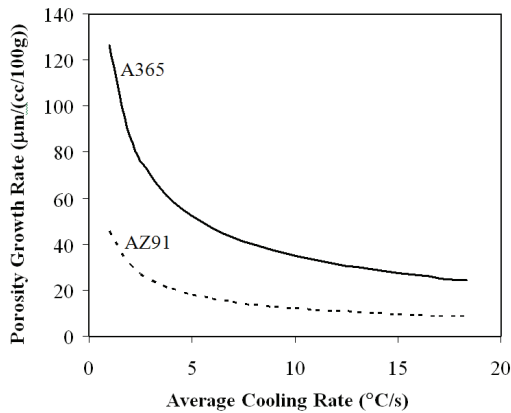


Figure 3. Porosity growth rate vs. cooling rate when the initial hydrogen content increases in the amount of 0.14 cc/100g for A356 (from 0.11 to 0.25 cc/100g) and AZ91 (from 17.72 to 17.86 cc/100g)

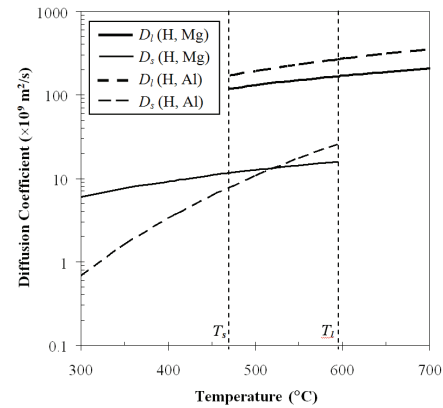


Figure 4. Diffusion coefficient of hydrogen in Mg and Al as a function of temperature {17}

Porosity and oxide films in AZ91

In this study, we examined the microstructure of magnesium alloy AZ91 ingots gravity-poured in plate graphite molds. Temperature data during cooling was acquired with type K thermocouples at 60 Hz in two locations of each casting. The microstructure of samples extracted from the regions of measured temperature was then characterized using optical metallography, tensile tests, and Scanning Electron Microscopy (SEM) of the fracture surfaces. The nature of oxide film and porosity defects in AZ91 was investigated.

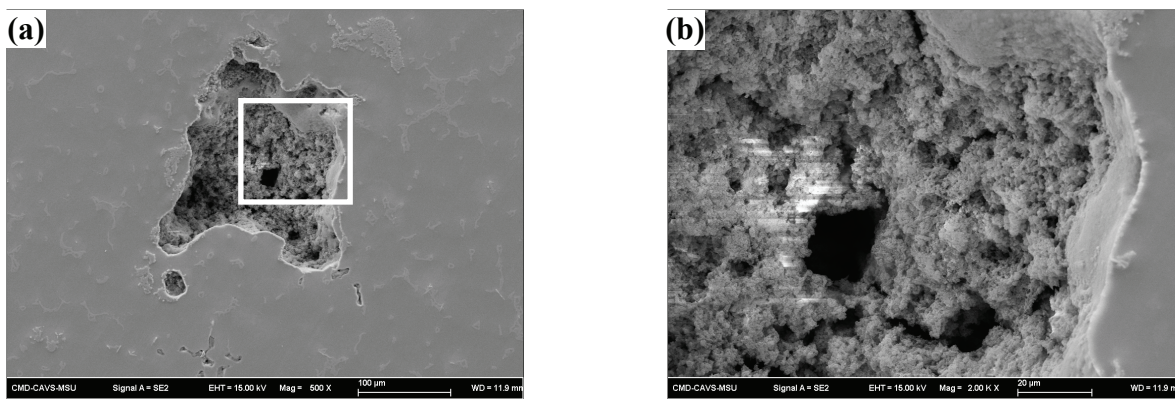


Figure 5 - (a) Typical pore morphologies formed at the location close to the thermocouple in casting AZ91 C1 sample; (b) higher magnification (2000X) of image (a).

Porosity was the major defect observed in the tested specimens. Pores ranging in size from 100 µm to 500 µm were found in many of the polished surfaces. Figure 5 shows typical pore morphology at a location close to the thermocouple in the AZ91 C1 sample. A magnified view (Fig. 5(b)) reveals dendrites protruding into the pore as well as pieces of oxides on the surface of the pore. EDX spectroscopy shows a three-fold increase of the oxygen content inside the pore compared with the surrounding matrix. This pore was most probably caused by interdendritic shrinkage; however, the presence of oxides might suggest also a pore formed by an entrained

double oxide that was torn apart by shrinkage-induced shear forces. The details of fracture surfaces of tensile test AZ91 samples are shown in Figures 6 and 7. Figure 6 shows two symmetrical oxide films on either side of a fracture surface. This agrees well with the observation by Griffiths and Lai [16] for pure Mg castings. A magnified view of the oxide region (Figure 7) reveals a pleated surface, similarly as observed in double oxide films in aluminum alloys.

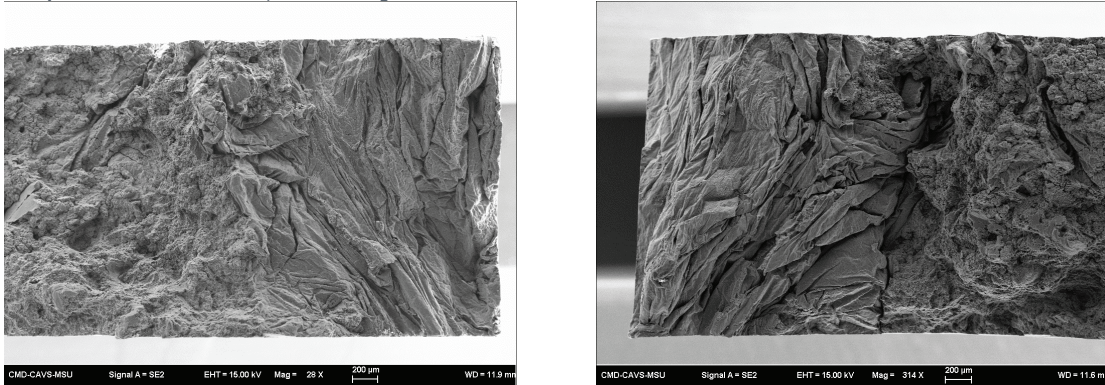


Figure 6 - Scanning electron microscope images of oxide films on the two sides of the fracture surfaces of a tensile test specimen taken from AZ91 sample C1.

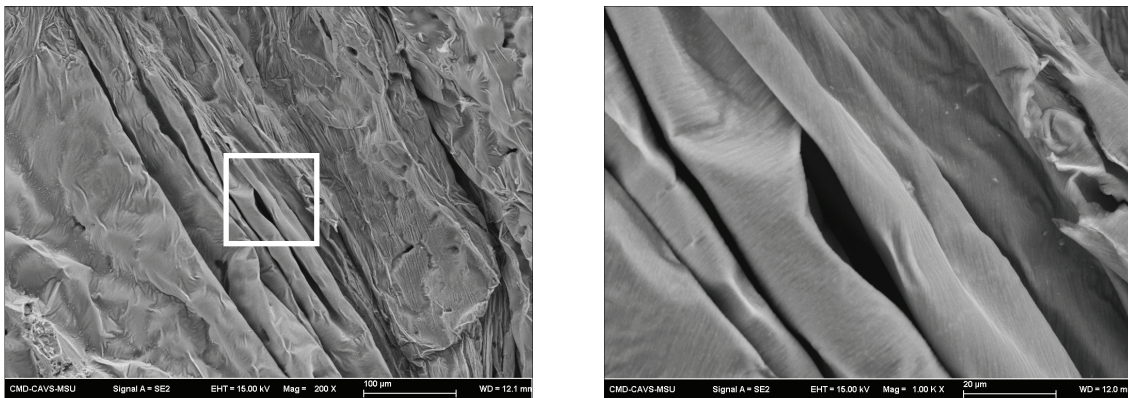


Figure 7. Higher magnification views of the oxide film found on the fracture surface shown in Fig. 6.

Porosity and oxide films in AE42

In this study, we examined the microstructure of magnesium alloy AE42 ingots gravity-poured in plate graphite molds. Two graphite plate molds and a ceramic cylindrical mold were selected to produce a wide range of cooling rates. Temperature data during cooling was acquired with type K thermocouples at 60 Hz in two or three locations of each casting. The microstructure of samples extracted from the regions of measured temperature was then characterized with optical metallography. This work investigated the nature of oxide film and porosity defects in AE42 for different cooling rates.

The tested AE42 alloy composition was Mg, 3.96%Al, 0.35%Mn, 0.01%Si, 0.001%Ni, 0.007%Zn, 0.0003%Fe, 0.0008%Cu, and 8ppm Be. The furnace charge was in the form of pre-alloyed ingot. The weight of the melt was 8 kg and the alloy was melted in an electrical resistance furnace. For protection, Ar and CO₂+3%SF₆ were used as cover gases. The pouring temperature for AE42 was approximately between 680 to 700 °C. No degassing procedures were used. All castings were poured from one melt. The melt was poured directly from the crucible to minimize temperature decrease during pouring.

The pouring temperature was approximately 715, 695, and 725 °C for castings type C, A, and E. All the molds were not preheated and were coated with boron nitride. In order to assess the reproducibility of the results, two molds were used for each type of casting.

Temperature data was acquired with thermocouples type K at approximately 60 Hz. The cooling curves are shown in Figure 8. The cooling curves are labeled in the following format: xn_m, where x – is a letter, indicating the mold type, n – indicates casting number (1 or 2), m – indicates thermocouple (1 or 2) for molds A and E and position of thermocouples for molds type C (b-bottom of casting, c-center of casting). The cooling curves show an excellent reproducibility. The data measured by the thermocouple near the top of the casting was discarded because of turbulence in this region. As shown in Figure 8, the cooling rates for AE42 alloy castings were approximately 20, 5, and 1 °C/s for molds A, C, and E, respectively.

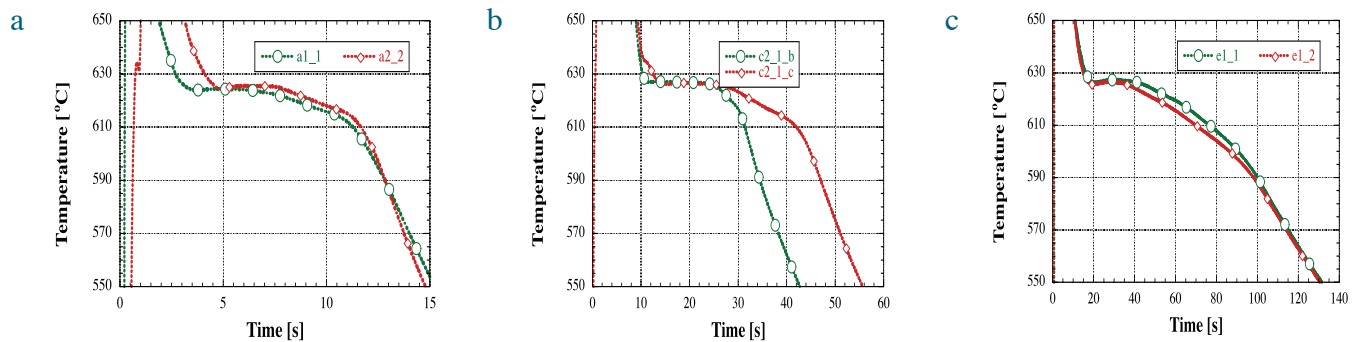


Figure 8. Cooling curves for AE42 Mg alloy castings. (a) mold type A, (b) mold type C, (c) mold type E.

A common feature found in all the samples is that the pores were observed to be smaller at higher cooling rates. Porosity was the major defect observed in the tested specimens. Figure 9 shows long pieces of oxide films, some longer than 1 mm in the sample E1-1 from the mold type E with cooling rate of 1 °C/s. The distinct precipitation upon both sides of the film might suggest the former existence of a double oxide that was later torn open, with the higher precipitation occurring on the wetted side. It is interesting to note that oxide films were found only in the samples from ingots cast at the lowest cooling rate. This fact needs confirmation by examining more samples.

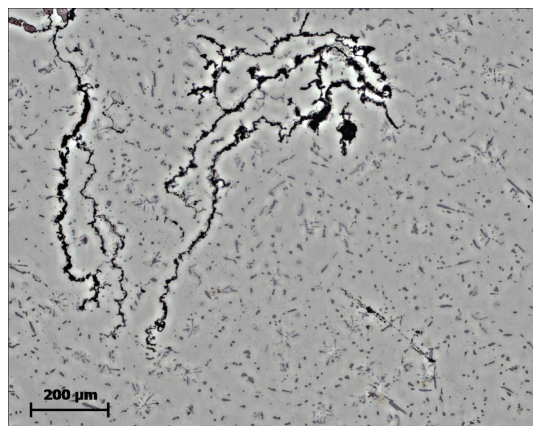


Figure 9. Typical micrographs of sample E1-1, showing porosity and oxide films.

Dendrite growth model in magnesium alloy

In this work, a coupled cellular automaton (CA) - finite element (FE) model was developed to simulate the dendrite growth during the solidification on magnesium alloy, AZ91. The model was applied to the simulation of small specimens with equiaxed and columnar grain growth. The influence of cooling rate and some kinetics parameters on the grain morphology were also discussed as follows.

A single nucleus is set at the calculation domain center to start the grain growth process during solidification. The calculation domain has uniform initial temperature and composition. Constant heat flux ($10\text{kw}/\text{m}^2$) is imposed at the four walls. The nucleus has an initial composition kC_0 and preferred growth orientation of zero degree with respect to the horizontal direction. The square domain has a 400×400 mesh and a side length of $200 \mu\text{m}$. Figures 10(a), (b), and (c) respectively presents the simulated evolution of equiaxed dendrite growth at different holding times of 0.0212s, 0.0424s, and 0.0636s. It can be seen that in the early stage of solidification, the dendrite develops the primary arms which follow the crystallographic orientations (Figure 10(a)). As solidification proceeds, the primary arms become larger and the secondary arms begin to occur (Figure 10(b)). With further solidification, some tertiary dendritic arms form from the second arms (Figure 10(c)).

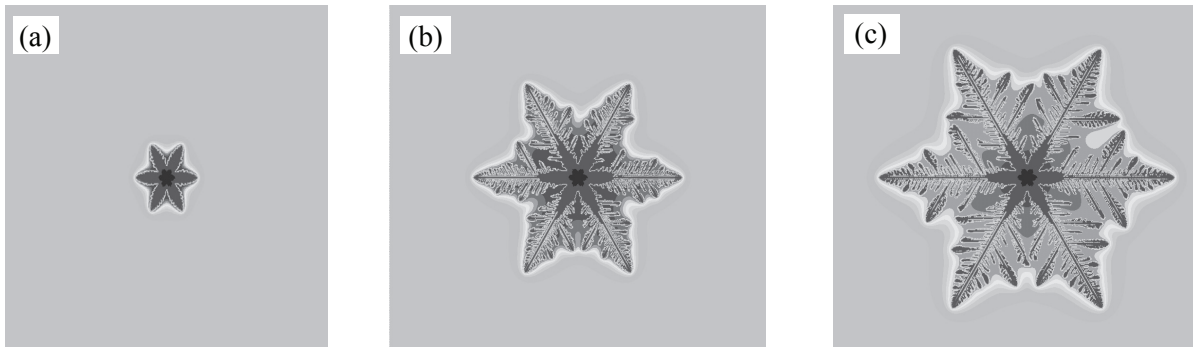


Figure 10. Solute map at different holding time. (a) 0.0212s, (b) 0.0424s, (c) 0.0636s

Two different heat flux boundary conditions were imposed on the walls to study the influence of cooling rate on dendrite morphology. Large heat flux corresponds to high cooling rate. An increase of the heat flux makes the dendrite grow faster and the secondary arms longer. As Figure 11 (b) shows, when the heat flux is $5\text{kw}/\text{m}^2$, only a few secondary arms occur. In addition, a large heat flux makes the grain grow faster, so more solute is released from the solid and there is less time for solute diffusion, which produces a high solute composition in the liquid.

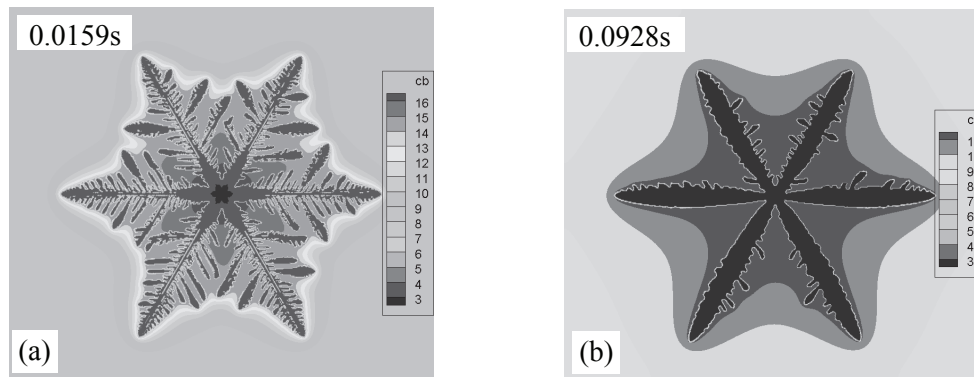


Figure 11. Solute map with heat flux of (a) $20\text{kw}/\text{m}^2$; (b) $5\text{kw}/\text{m}^2$

The growth of columnar dendrites was also simulated for the same Mg alloy directionally solidified with heat flux applied on the left wall. The calculation domain has a 400×200 mesh and dimensions of $100 \times 50 \mu\text{m}$. Two nuclei were placed at the left wall with crystallographic orientation aligned with the temperature gradient.

Figures 12 (a) and (b) respectively present the simulated evolution of columnar dendrites with heat flux of $80\text{kw}/\text{m}^2$ and $20\text{kw}/\text{m}^2$. A larger heat flux produces a steeper temperature gradient which leads to thinner dendrites. The primary arms whose morphology orientation is not parallel to the heat transfer direction will be stopped by the growth of the arm parallel to temperature gradient. The growth of some main arms can also be stopped by nearby dendrites. High liquid composition between the two columnar grains due to the small separation between them makes the second arms comparatively short.

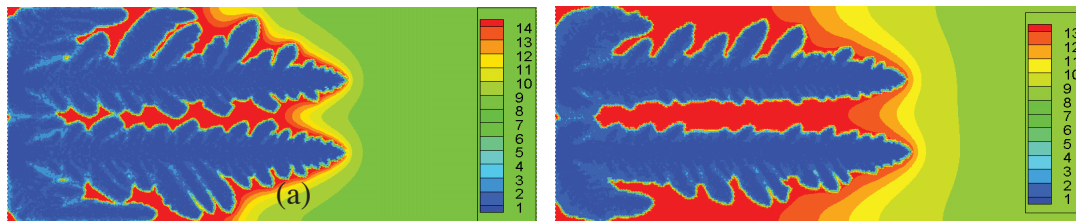


Figure 12. Solute map with heat flux of 80kW/m² and holding time 0.0339s (a) and 20kW/m² with holding time 0.1166s (b)

Conclusions

In this study, the following conclusions were derived:

- Solidification-Porosity model developed based on transport of inclusions and hydrogen diffusion pore growth. Model validated for A356. Simulations performed for AZ91.
- A dendrite growth model based on the cellular automaton technique was developed, which shows good potential to deal with the still unsolved problem of mesh-induced anisotropy in hexagonal systems like Mg alloys.
- Gravity-poured castings of AZ91 and AE42 were performed in graphite and ceramic molds of various sizes. Analysis of microstructural data (in progress) should provide an estimate of correlation of porosity vs. cooling rate, useful for model verification (though no hydrogen content data is available).
- Microstructural analysis of AZ91 and AE42 samples revealed the presence of oxide films similar to those found in Al castings, including some in the interior surface of pores.
- It is important to emphasize that the porosity study performed in this work is a “local” analysis of the solidification phenomena affecting porosity formation, in which the presence and features of porosity was correlated with local variables as cooling rate, temperature gradient, content of oxides, etc; independently of the process conditions that caused those local variables. Therefore, although performed in the context of gravity-poured castings, the analysis is not limited to this particular process.

References

1. C.H. Caceres, C.J. Davidson, J.R. Griffiths, and C.L. Newton, “Effects of Solidification Rate and Ageing on the Microstructure and Mechanical Properties of AZ91 Alloy,” *Materials Science and Engineering A*, 325 (2002), 344-355.
2. A.S. Sabau and S. Viswanathan: *Metall. Mater. Trans. B*, 2002, vol. 33B, pp. 243-255.
3. P.D. Lee, A. Chirazi, R.C. Atwood and W. Wang: *Mater. Sci. Eng. A*, 2004, vol. 365B, pp. 57-65.
4. K.D. Carlson, Z. Lin and C. Beckermann: *Metall. Mater. Trans. B*, 2007, vol. 38B, pp. 541-555
5. D.M. Stefanescu: *Int. J. Cast Met. Res.*, 2005, vol. 18, pp. 129-143.
6. John Campbell, *Castings* 2nd ed. (Butterworth-Heinemann, London, 2003), 17-69.
7. X. Yang, X. Huang, X. Dai, J. Campbell, and R. J. Grant, “Quantitative Characterization of Correlations between Casting Defects and Mechanical Strength of Al-7Si-Mg Alloy Castings,” *Materials Science & Technology*, 22 (2006), 561-570.

8. J. Campbell, "Entrainment defects," *Materials Science & Technology*, 22 (2) (2006), 127-145.
9. J. Knott, P.R. Beeley, J.R. Griffiths, N.R. Green, C.J. Newton, and J. Campbell, "Commentaries on 'Entrainment Defects' by J. Campbell," *Materials Science & Technology*, 22 (2006), 999-1008.
10. R. Raiszadeh, and W.D. Griffiths, "A Method to Study the History of a Double Oxide Film Defect in Liquid Aluminum Alloys," *Metallurgical and Materials Transactions. B*, 37 (2006), 865-871.
11. J. Mi, R.A. Harding, M. Wickins, and J. Campbell, "Entrained Oxide Films in TiAl Castings," *Intermetallics*, 11 (2003), 377-385.
12. S.D. Felicelli, D.R. Poirier and P.K. Sung: *Metall. Mater. Trans. B*, 2000, vol. 31B, pp. 1283-1292.
13. S.D. Felicelli, J.C. Heinrich and D.R. Poirier: *Int. J. Numer. Meth. Fluids*, 1998, vol. 27, pp. 207-227.
14. Q.T. Fang and D.A. Granger: *AFS Trans.*, 1989, vol. 97, pp. 989-1000.
15. Wang, L., H. Rhee, Felicelli, S.D., Sabau, A.S., Berry, J.T., "Oxide Film and Porosity Defects in Magnesium Alloy AZ91," 2009 TMS Annual Meeting & Exhibition, Shaping Casting: Third International Symposium, San Francisco, CA, Feb 15-19, 2009 (in review)
16. W.D. Griffiths, and N.W. Lai, "Double Oxide Film Defects in Cast Magnesium Alloy," , 38 (2007), 190-196.
17. (See #3 in Publication list)

Presentations/Publications/Patents

Publications resulting from this project:

- H. Yin and S.D. Felicelli, "A cellular automaton model for dendrite growth in magnesium alloy AZ91", *Modeling and Simulation in Materials Science and Engineering*, vol. 17, p. 075011 (2009)
- C.M. Pita and S.D. Felicelli, "Fluid-solid interaction problems with thermal convection using the immersed element-free Galerkin method", *International Journal for Numerical Methods in Fluids*, vol. 62, pp. 1-23 (2010)
- Felicelli, S.D., Wang, L., Pita, C.M., Escobar de Obaldia, E., "A model for Gas Microporosity in Aluminum and Magnesium Alloys", *Metallurgical and Materials Transactions B*, vol. 40B, pp. 169-181 (2009)
- Wang, L., H. Rhee, Felicelli, S.D., Sabau, A.S., Berry, J.T., "Oxide Film and Porosity Defects in Magnesium Alloy AZ91," *Shape Casting: The 3rd International Symposium*, eds. J. Campbell, P.N. Crepeau and M. Tiryakioglu, TMS, Warrendale, PA, 2009, pp. 123-130
- Wang, L., H. Rhee, Felicelli, S.D., Sabau, A.S., Berry, J.T., "Interdependence between Cooling Rate, Microstructure and Porosity in Mg alloy AE42," *Magnesium Technology*, eds. E.A. Nyberg, S.R. Agnew, N.R. Neelameggham and M.O. Pekguleryuz, TMS, Warrendale, PA, 2009, pp. 249-253
- H. Yin and S.D. Felicelli, "Simulation of microstructure evolution during solidification of magnesium alloys", *Materials Processing Fundamentals*, edited by P. Anyalebechi, TMS (The Minerals, Metals & Materials Society), 2009, Warrendale, PA, pp. 627-634

U.K. Sajja and S.D. Felicelli, "Element-free Galerkin method for thermosolutal convection and macrosegregation", International Journal for Numerical Methods in Fluids, in press, doi: 10.1002/flid.2169 (2009)

C.M. Pita and S.D. Felicelli, "A fluid-structure interaction method for highly deformable solids", Computer and Structures, vol. 88, pp. 255-262 (2009)

J.C. Heinrich, U.K. Sajja, S.D. Felicelli, D.G. Westra, "Projection method for flows with large local density gradients. Application to dendritic solidification", International Journal for Numerical Methods in Fluids, vol. 57 (9), pp. 1211-1226 (2008)

S. Poola, S.D. Felicelli, S. Legget, J.T. Berry: "A re-examination of factors affecting porosity gradients in unidirectionally solidified samples", Transactions of the American Foundry Society, vol. 116, pp. 157-168 (2008)

S.D. Felicelli, E. Escobar de Obaldia and C.M. Pita, "Simulation of hydrogen porosity during solidification", Transactions of the American Foundry Society, vol. 115, paper 07-078, pp. 1-13 (2007). BEST PAPER AWARD

S. Felicelli, J. Berry, R. Cuesta, R. Luck, R. Lett: "An international collaboration for the study of defects in castings", 2008 ASEE Annual Conference & Exposition, Pittsburgh, PA, June 22 - 25, 2008

S. Felicelli, C. Pita and E. Escobar de Obaldia, "Modeling the onset and evolution of hydrogen pores during solidification", Shape Casting: The 2nd International Symposium, edited by P. Crepeau, M. Tiryakioglu and J. Campbell, TMS (The Minerals, Metals & Materials Society), ISBN: 978-0-87339-660-8, 2007, pp. 201-208

E. Multi-Material Metallurgical Bond Joining to Steel

Principal Investigator: Qingyou Han
Purdue University
Mechanical Engineering Technology Department
401 North Grant Street
Knob Hall - Room 129
West Lafayette, IN 47907-2021
(765) 494-5866; e-mail: hanq@Purdue.edu

Technology Area Development Manager: William Joost
(202) 287-6020; e-mail: william.joost@ee.doe.gov

Field Project Officer: Magda A. Rivera
(304) 285-1359; email: magda.rivera@netl.doe.gov

Participants

This project is being conducted as a partnership with USAMP-MMV with participation that includes the following automotive company representatives:

Bill Charron, Ford Motor Company; e-mail: wcharron@ford.com_(Project Leader)

Steve Logan, Chrysler Corporation; e-mail: sl16@chrysler.com

Larry Ouimet, General Motors Corporation; e-mail: larry.j.ouimet@GM.com

Contractor: United States Automotive Materials Partnership
Contract No.: DE-FC26-02OR22910

Objectives

- The primary objective of this concept feasibility project is to verify that the proposed technology can achieve a true metallurgical bond between cast aluminum and steel and between cast magnesium and steel. There are no known alternative, economically attractive processes that can achieve a true metallurgical bond.
- The metallurgical bond between magnesium and aluminum will also be assessed.
- Technical hurdles to implementation will be identified for potential follow-on work.

Approach

- The project team will create test criteria and identify potential target applications.
- Test piece castings will be designed for selected inserts that meet the test criteria.
- Dr. Han will develop the process for and manufacture the test castings.
- The cast components will be tested according to the test procedure and analyzed by the team.
- Technical hurdles to implementation will be identified for potential follow-on work.
- Information and data will be distributed to the participating companies.

Accomplishments

- The Test Criteria Team was established with Original Equipment Manufacturers and supplier participants.
- The Test Criteria Team identified potential applications for the technology to be developed for joining aluminum to steel, magnesium to steel and aluminum to magnesium. Included in the Potential Components List were the anticipated cast materials and insert descriptions.
- In light of the first Potential Components List exercise, the team identified the casting materials and insert materials to be considered for the test castings to be produced by Dr. Han.
- The Team established the testing criteria.
- Three casting design's were created to meet all the test criteria established.
- Development has shown that a strong metallurgical bond can be achieved with this technology for steel pins in cast aluminum and a steel strap to a cast disc.
- Design #1 test castings, steel pin in magnesium, were tested at Purdue and did not indicate a metallurgical bond was achieved. It was concluded an additional step might be required like pre-coating the steel pin with aluminum prior to casting into the magnesium. The same results occurred with the steel strap and magnesium disc.
- A few castings of Design #3 of cast magnesium to cast aluminum were made. Evidence of a metallurgical bond was indicated visually but physical and metallurgical evaluation could not be concluded prior to cessation of project work at the direction of USAMP.
- Technical hurdles to implementation have been identified for potential follow-on work.

Future Directions

A follow-on project proposal has been prepared for consideration by USAMP focusing on the following technical hurdles to implementation:

- Determine that the ultrasonic method can deliver a metallurgical bond in a steel mold
- Develop a predictive frequency modeling tool for optimization and understanding of the sound distribution during the bonding process
- Optimize the ultrasonic method for metallurgical bonding of aluminum to steel and magnesium to aluminum considering the following variables:

Frequency

Ultrasound duration

Insert pre-heating

Bond area

Metal temperature

Introduction

The pressure to reduce weight and improve fuel economy has resulted in increased numbers of cast aluminum and magnesium components that need to be attached to the existing steel architectures. The joining of these multi-material components requires traditional bolted connections, mechanical locking strategies or other non-traditional welding processes. These joining solutions result in added costs and potential offsetting mass (bolts, bosses, flanges, etc.) Capital costs may be increased to implement non-traditional welding processes, machining processes, fastener assembly stations, associated material handling systems, etc. Operating costs also increase due these added processes and added parts. In addition, some of the mass reduced by using the lighter weight materials is offset by added locking features, bolts, bolt bosses, flanges and other features. Recent investigative development at Oak Ridge National Laboratory has shown that it is possible to achieve a metallurgical bond between aluminum and steel or magnesium and steel by applying ultrasound to steel inserts in molds for casting of the lighter metals. The initial work seemed to indicate that there was no significant loss in productivity due to the introduction of the insert or ultrasound. However, significant development and testing is needed to verify these assumptions and identify the risks and opportunities for application of this technology.

This project proposes to develop and evaluate a new concept in bonding cast aluminum and magnesium components to steel. The new concept creates a metallurgical bond when ultrasound is applied to a steel insert, (sheet, tube, rod, etc.) during the casting process without significant alteration to the casting cycle time or process. It is envisioned that the development of this technology could result in cast components with weldable steel inserts that could be joined to today's steel architectures by currently available, economical production processes like spot welding.

The development approach will build upon preliminary work done at Oak Ridge National Laboratory. Test castings will be made with this new technology, tested and evaluated. In addition, technical hurdles to implementation will be identified for potential follow-on work.

Work Completed

Task 1: Establish Team, Confirm Target Applications & Create/Identify Test Criteria

Approach:

1. Establish Team
2. Define potential applications for the technology to be developed for joining Al to steel and Mg to steel.
3. Select an Al and Mg alloy.
4. Define metrics of success and attributes of a good bond (physical properties, metallurgical properties, and corrosion performance). Criteria to be considered:
 - Features required for test piece
 - Bond line interface quality
 - Diffusion layer distance
 - Brittleness
 - Raw Strength

- Key life testing
- Pull-out/shear
- Peel
- Fatigue
- Porosity
- Corrosion performance
- Process parameters (i.e. time to produce metallurgical bond, ultrasonic control and measurement aspects, etc.)
- Requirements for steel sample preparation
- Etc.

Deliverables:

- Team established
- Potential application(s) (flanges, tubes, etc.) defined.
- Testing criteria and metrics of success defined.
- Requirements for the casting design and insert(s) defined.

Results:

The Test Criteria Team was established and functioning with active participation from:

- Chrysler
- Ford
- General Motors
- Purdue
- Tech Knowledge

The Test Criteria Team identified potential applications for the technology to be developed for joining aluminum to steel, magnesium to steel and aluminum to magnesium. Included in the Potential Components List were the anticipated cast materials and insert descriptions. The Potential Components List is included in the Appendix to this report.

The Team settled on the following testing criteria for analyses of the test castings:

- Cross sectioning
- Torsional force
- Pull or push force (depending on bond to be tested)
- Die penetrent
- Stress/strain
- Peel

Based upon the work completed in the first task, the team identified the casting materials and insert materials to be considered for the test castings to be produced.

Table 1. Casting and Insert Materials Under Consideration

Casting Material	Insert
Magnesium AZ91E	Mild steel weldable flange
Aluminum 356	Mild steel weldable flange
Magnesium AZ91E	Steel rod
Aluminum 356	Steel rod
Magnesium AZ91E	Aluminum 6061 rod
Magnesium AZ91E	Aluminum 356 cast material

Task 2: Design Test Casting and Steel Inserts:

Approach:

Design the test casting and steel insert(s) to satisfy testing criteria establish in Task 1.

Deliverables:

- Casting design completed.
- Insert(s) design completed.

Results:

The Test Criteria Team identified three casting designs that would achieve all the objectives established in Task 1. The three designs are:

Design #1:

The design 1 is illustrated in [Figure 1](#). An insert will be cast in with a cylindrical casting. The test casting will be tested for shear strength and fatigue. Three combinations of metals will be made: steel insert in Mg casting, steel insert in aluminum casting, and aluminum insert in Mg casting. For each combination, 15 samples will be made and shipped to USCAR for testing.

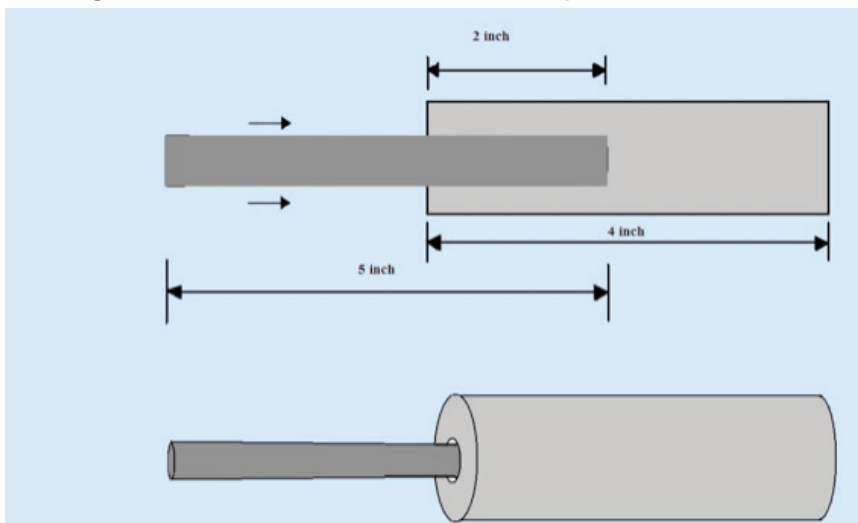


Figure 1. Test Casting Design #1.

Design #2:

Design 2 is illustrated in Figure 2. A steel or aluminum strap will be joined to an aluminum or magnesium disc casting. Testing will be carried out to determine the interfacial strength between the strap and the 2 inch diameter puck. Three combinations of metals will be made: steel strap with Mg casting, steel strap with aluminum casting, and aluminum strap with Mg casting. For each combination, 15 samples will be made and shipped to USCAR for testing.

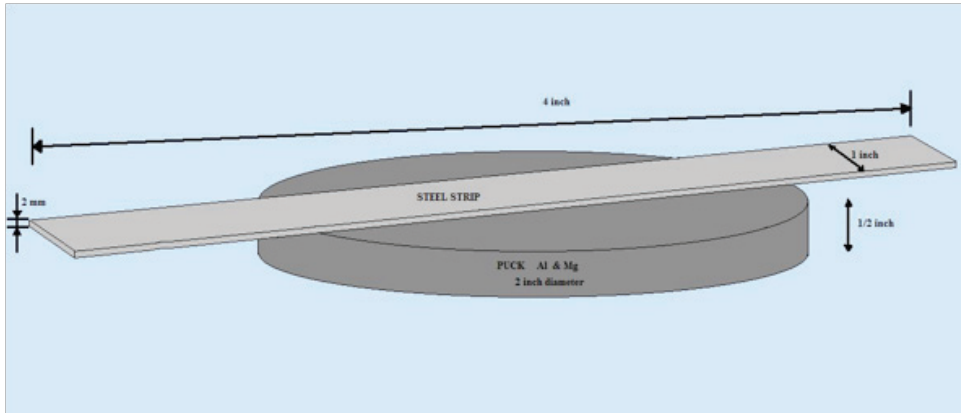


Figure 2. Test Casting Design #2.

Design #3:

Design 3 is illustrated in Figure 3. This design will be used to test bi-metal casting. An aluminum casting (half a disc) will be made in a mold. Molten Mg alloy will then cast to make a disc half Al and half Mg. The joint between the aluminum half and the Mg half will be tested. 15 specimens will be made and shipped to USCAR for further testing.

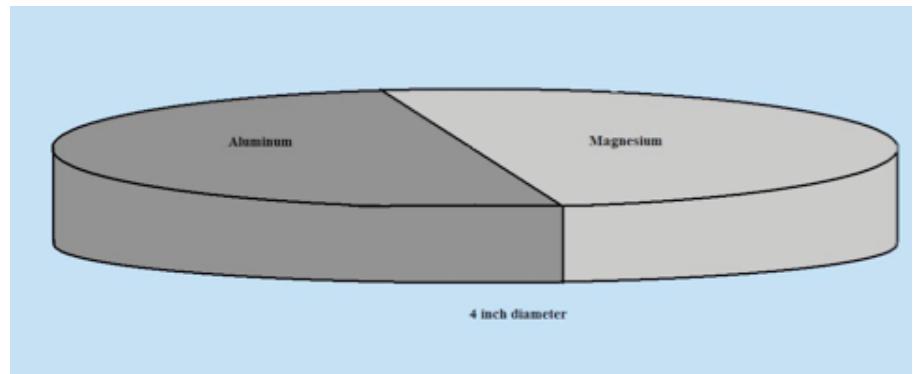


Figure 3. Test Casting Design #3.

Task 3: Develop Process and Make Test Pieces

Approach:

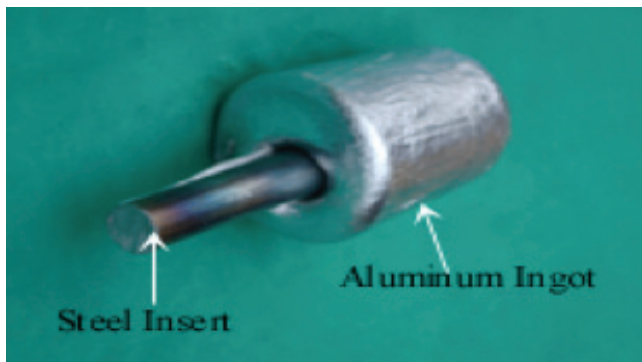
- Prepare mold and ultrasonic tooling (simple molds will be used during this task)
- Procure materials
- Prepare inserts
- Develop the process for manufacturing the test pieces
- Manufacture test pieces
- Document process data

Deliverables:

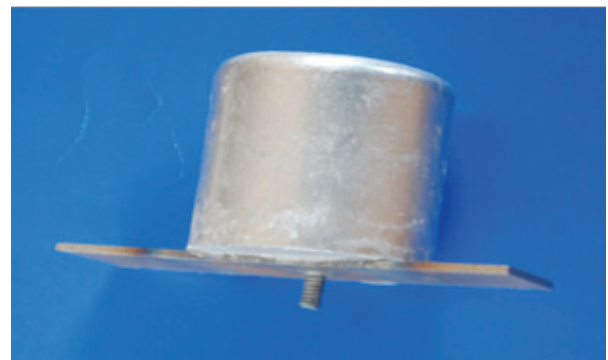
- Mold and ultrasonic tooling prepared and ready for casting process.
- Samples ready for visual, material and/or property evaluations.
- Data set captured.

Results:

- Design #1 test castings, steel pin in aluminum and steel pin in magnesium, were manufactured and distributed for testing. **Figure 4 (a)** shows a Design #1 test casting.
- Design #2 test castings, steel strip on aluminum, were manufactured and distributed for testing. **Figure 4 (b)** shows a Design#2 test casting.
- Design #3 test castings, bi-metal aluminum to magnesium, were manufactured.



Design #1 Casting



(b) Design #2 Casting

Figure 4. Test castings made in this project

Task 4: Test and Evaluate Test Pieces

Approach:

Test, evaluate, analyze and verify that the new casting/joining process can achieve metallurgical bond between Al to steel and Mg to steel as defined in Task 1. Evaluations will consider physical/mechanical and metallurgical properties and corrosion performance.

Deliverable:

Test results and analyses of the capability of this technology to bond multi-material structures were completed.

Results:

- Design #1 test castings, steel pin in aluminum, were tested by Ford and CTC. **Figure 5** shows the Ford specimen template and **Figure 6** shows the Ford test setup with a specimen. Micrographs and physical testing indicated a metallurgical bond was achieved with evidence of tearing of aluminum during the push out (shear stress) testing. Micrographs indicated a transitional zone between the aluminum and steel at the joint, shown in **Figure 7**.
- Design #1 test castings, steel pin in magnesium, were tested at Purdue and did not indicate a metallurgical bond was achieved. It was concluded an additional step might be required

like pre-coating the steel pin with aluminum prior to casting into the magnesium.

- Design #2 test castings, steel strap to aluminum puck, were tested by Ford. Micrographs and physical testing indicated a metallurgical bond was achieved with evidence of tearing of aluminum during the peel test (shear stress).
- Design #2 test castings, steel strap to magnesium puck, were tested at Purdue and did not indicate a metallurgical bond was achieved. Again, it was concluded an additional step might be required like pre-coating the steel pin with aluminum prior to casting into the magnesium.
- Design #3 test castings, bi-metal castings, magnesium to aluminum, were visually analyzed for evidence of a metallurgical bond at Purdue and by the project team. It was apparent that a bond existed but no physical testing occurred.
- Due to a conflict with the USAMP Cooperative Agreement and the funding procedure for this project, all work was ended prior to completion of the Test and Evaluation Task.

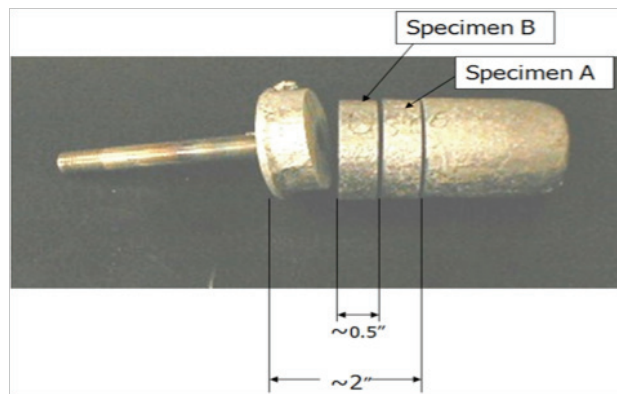


Figure 5. Ford Specimen Template.

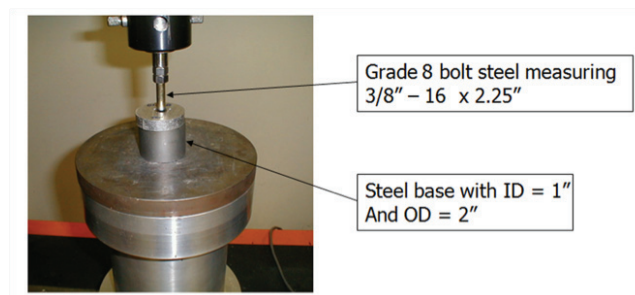
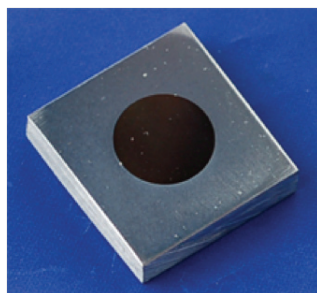
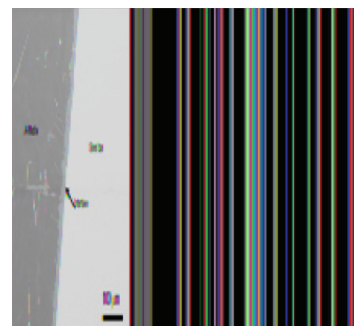


Figure 6. Ford test setup with a specimen



(a)



(b)

Figure 7. Defect-free metallurgical bond has been obtained using the new method. (a) Polished samples, and (b) SEM image of the bond.

Task 5: Information Dissemination and Reporting

Approach:

- Identify technical hurdles to implementation
- Disseminate technology to team members

Deliverables:

- Annual and Semi-Annual Reports
- Identification of hurdles to implementation

Results:

- Technical hurdles list created and maintained and included in appendix to this report.
- All results distributed to team and maintained on USCAR V-Room secured virtual information site.

Conclusions

The results of the development and evaluation conducted during this project indicate the concept is a viable means to bond steel to cast aluminum. Evidence was shown that a metallurgical bond could also be achieved between aluminum and magnesium, though no physical testing was conducted. Testing indicated the ultrasonic method did not achieve a direct metallurgical bond between steel and cast magnesium without added process steps. The team has identified a broad number of potential applications for this technology that could result in weight and cost reductions in the fastening of lightweighting materials to vehicle structures. With the successful development of this technology it is clear that lightweighting materials such as aluminum and magnesium will be enabled for increased usage.

F. Corrosion of Magnesium Alloy in the Southern Regional Center for Lightweight Innovative Designs (SRCLID)

Principal Investigator: Mark Horstemeyer
CAVS Chair Professor in Computational Solid Mechanics
ASME Fellow; Mechanical Engineering
Mississippi State University, P.O. 5405
Mississippi State, MS 39759-5405
Phone: (662) 325-5449; email: mfhorst@cavs.msstate.edu

Participants: S. Groh, H. Martin

Technology Area Development Manager: William Joost
(202) 287-6020; e-mail: william.joost@ee.doe.gov

Project Manager: Magda Rivera
(304) 285-1359 ; e-mail: magda.rivera@netl.doe.gov

Contractor: Mississippi State University
Contract No.: DE-FC26-06NT42755

Objective

- Understand and model the mechanisms of corrosion and hydrogen embrittlement in Mg alloys.

Approach

- Generate experimental data to quantify the mechanism of corrosion in Mg alloy.
- Characterize molecular dynamics of hydrogen embrittlement to quantify the effect of hydrogen on dislocation properties and void growth in Mg.
- Development of a macroscopic model for corrosion.

Accomplishments

- Identified mechanisms at the origin of the plastic flow in a Mg single crystal with a pre-existing pore.
- Developed a Mg potential for dislocation purposes and of the pair Mg-H to model hydrogen effects.
- Characterize the effect of hydrogen on the dislocation core structures.
- Determine the most corrosive salt spray environment based on coupon changes, including thickness, weight, and pit characteristics such as pit number density, pit area, nearest neighbor radius, and intergranular corrosion area fraction.
- Compare the corrosion mechanisms of a 3.5% NaCl aqueous solution on as-cast AE44 Mg using immersion testing technique and the most corrosive salt spray testing environment previously determined over 60 hours.

Future direction

- Determine the effect of hydrogen on the dislocation Peierls stress and mobility.
- Determine the effect of hydrogen on void growth.
- Expand results to explain corrosion in other magnesium alloys, such as AM60 and AZ91.
- Demonstrate the mechanisms for corrosion in magnesium alloys exposed to mechanical stresses.

Introduction

Understanding the corrosion mechanisms that ultimately lead to the failure of metals is of utmost importance. Magnesium is currently being investigated for use in the aerospace and automobile industries, but its high corrosion rate relegates it to locations unexposed to the environment (Makar and Kruger (1993); Song and Atrens (2003)). Because of its electrochemical potential as illustrated by the galvanic series, magnesium alloys corrode quickly when exposed to saltwater (Shaw (2003)). Furthermore, the presence of rare earth elements, such as cerium, in the eutectic regions surrounding the grains of AE44 can also lead to galvanic corrosion (Alvarez et al. (in review); Bakke and Westengen (2005)). Understanding the corrosion mechanisms of pitting, intergranular corrosion, and general corrosion could help control corrosion in the future.

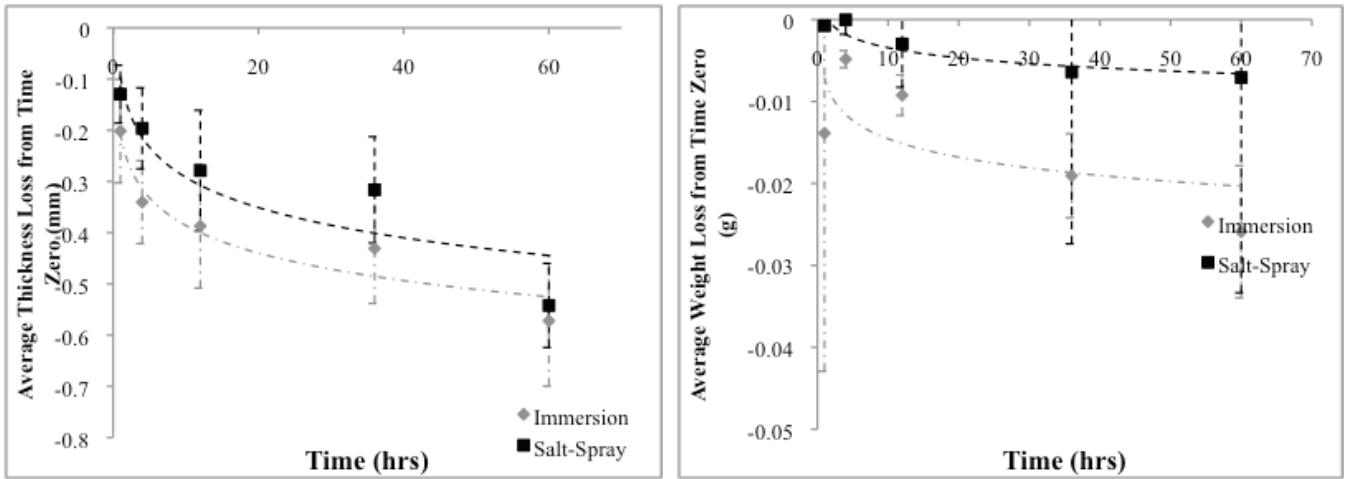
The current study was designed to determine the most corrosive test environment in the salt spray cabinet, while also taking into account the current issues with a continuous salt spray. Following this set of experiments, the most corrosive test environment determined experimentally was used alongside immersion testing to determine the corrosion mechanisms over time. Ultimately, the data gathered will be used to calibrate an Internal State Variable Model that will be used to predict the corrosion of magnesium alloys. The experimental set-up and main results for the comparison between immersion and salt spray are detailed in Section 2. In addition, the development of a magnesium interatomic potential using the Modified Embedded-Atom Method (MEAM) to accurately describe dislocation properties is detailed in Section 3. Concluding remarks are given in Section 4.

Comparing Immersion and Salt Spray Environments

Experimental Set-Up

Twelve coupons (25 mm x 25 mm) of similar thicknesses were cut from an AE44 Engine Cradle, with the as-cast material covering the largest sides. The as-cast specimens were divided into two groups of six coupons. The coupons were then weighed and measured using calipers to determine the initial characteristics of the coupons.

The coupons were placed in either an immersion test, consisting of an 3.5% NaCl aqueous solution in an aquarium with aerator to ensure adequate oxygen within the system, or a Q-Fog machine using equal times of 3.5% NaCl aqueous solution spray, 100% humidity, and drying phases. The samples were removed and analyzed after 1 hr, 4 hrs, 12 hrs, 36 hrs, and 60 hrs. The coupons were then rinsed in distilled water to remove any residual salt, dried, weighed, and measured for comparison to the initial characteristics. Optical micrographs and laser profilometry scans were then taken of the surfaces.



(A) (B)
 Figure 1. Average Thickness Loss (A) and Average Weight Loss (B) of the AE44 Coupons Based on Testing Environment.

Results

Figure 1(A) shows the average thickness for the coupons exposed to the immersion cycle and exposed to the salt spray cycle at $t_1 = 1$ hr, $t_2 = 4$ hr, $t_3 = 12$ hr, $t_4 = 36$ hr, and $t_5 = 60$ hr. The coupons followed the same trend with respect to the thickness lost due to corrosion, although the samples in the immersion test lost more thickness than the samples in the salt spray test.

Figure 1(B) shows the average weight loss for the coupons exposed to the immersion cycle and exposed to the salt spray cycle at $t_1, t_2, t_3, t_4,$ and t_5 . Similar to the average thickness loss, the coupons followed the same trend with respect to the weight lost due to corrosion, although the sample in the immersion test lost more weight than the samples in the salt spray test.

Figure 2(A) shows the pit number density for the coupons exposed to the immersion cycle and exposed to the salt spray cycle at $t_1, t_2, t_3, t_4,$ and t_5 . As one can see, more pits were formed on the immersion coupons as compared to the salt spray coupons. In addition, the immersion coupons followed a parabolic trend, first increasing before decreasing, while the salt spray coupons followed a third order polynomial trend, first increasing, then decreasing, then increasing (or reaching a steady state).

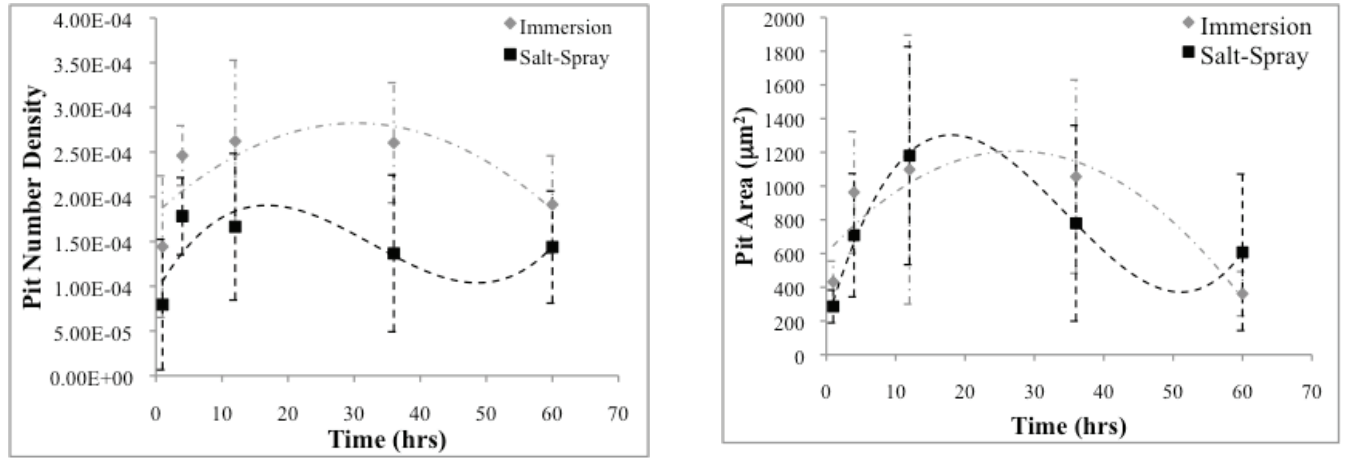
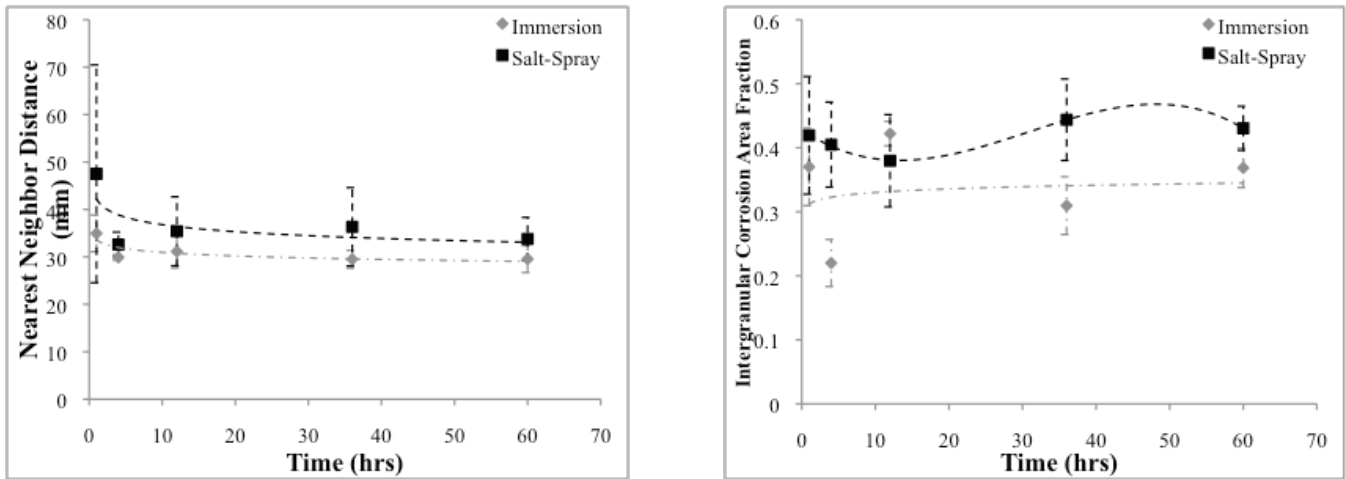


Figure 2. Average Pit Number Density (A) and Surface Area (B) of the AE44 Coupons Based on Testing Environment.

Figure 2(B) shows the pit surface area for the coupons exposed to the immersion cycle and exposed to the salt spray cycle at t_1 , t_2 , t_3 , t_4 , and t_5 . As with the pit number density, larger pits were present on the immersed coupons as compared to the salt spray cycles. The pit area also followed a parabolic trend for the immersed coupons and a third order polynomial trend for the salt-spray coupons.

Figure 3(A) shows the nearest neighbor distance for the coupons exposed to the immersion cycle and exposed to the salt spray cycle at t_1 , t_2 , t_3 , t_4 , and t_5 . There were larger distances between the pits on the salt spray coupons as compared to the immersed coupons. Both coupons, though, followed the same decreasing logarithmic trend as time proceeded.



(A) (B)
Figure 3: Average Nearest Neighbor Distance (A) and Intergranular Corrosion Area Fraction (B) of the AE44 Coupons Based on Testing Environment.

Figure 3(B) shows the intergranular corrosion area fraction for the coupons exposed to the immersion cycle and exposed to the salt spray cycle at t_1 , t_2 , t_3 , t_4 , and t_5 . There was more intergranular corrosion on the salt spray coupons as compared to the immersed coupons. Similar to the pit number density and pit area shown in Figure 2, a third order trend was observed for the salt spray coupons. However, the immersion coupons followed a logarithmic trend.

Relationship between Pitting Characteristics

The four figures, Figures 2 and 3 (A) and (B), illustrate the relationship between pit number density, pit area, and nearest neighbor distance. As the pit number density increases, the pit area also increases, as demonstrated with the immersion coupons and Figures 2(A) and 2(B). For the salt spray coupons, the pit number density and pit area follow the same trend. As the pit number density increases, the nearest neighbor distance decreases as the pits grow and coalesce. The following trends are evident in Figures 2 and 3: pit number density and pit area are proportionally related, while the nearest neighbor radius is inversely related to the pit number density and pit area. This result will be used for model development later.

Discussion

Figures 1(A) and (B) demonstrate that the most corrosive test method is the immersion cycle. This result is expected as the coupons were continuously exposed to aerated water, allowing all three corrosion mechanisms (pitting, intergranular, and general) to occur at the same time. The continuous presence of water also prevented build up of corrosion by-products on the surface, as the by-products were constantly removed. In general, pitting and intergranular corrosion, which have very little effects on thickness or weight, could occur simultaneously. The presence of water in the salt spray samples allowed for all three corrosion mechanisms to occur; the

drying portion of the salt spray cycles stopped both general and intergranular corrosion. Pitting corrosion continued during the drying portion of the cycle because water was trapped in small pits, allowing that corrosion mechanism to continue.

Figures 2-3 show the changes in pit characteristics. Over time, the chloride ions allowed the pits to grow, approaching more neighbors. General corrosion also affected the pit size by removing magnesium in even amounts from the entire surface; this allowed the portion of the pits “hidden” beneath the corrosion debris to become exposed, increasing the pit area. When the pit number and pit area decreased, general corrosion “caught” pitting corrosion, reducing the amount of magnesium surrounding the pits to the bottom of the pits present.

The salt spray coupons had fewer pits, but the pit area was not significantly different when compared to the immersed coupons. While water and chloride ions are necessary to initiate pitting, once the pit forms, it is autocatalytic (Fontana (1986)). Corrosion debris is formed, which can trap chloride ions and water beneath the surface. When the drying phase occurs, no additional pits can form, but the pits previously formed can continue growing. When the water is added in the second time period, the corrosion debris is removed, exposing the expanded pits (Figure 2(B)). The presence of water in the longer time periods (t_3 , t_4 , and t_5) allows general corrosion to occur. The drying cycle means general corrosion is stopped; when the salt spray cycle begins again, pits can form on the areas where general corrosion removed some of the magnesium surface. The cycling between salt spray, humidity, and drying implies that pitting occurs with the same amount comparable to the general corrosion. It is the cycling between corrosion mechanisms that result in the increase or decrease in pit number density and pit size. Note that as a pit forms during the salt spray phase, it shrinks during the humidity phase and grows during the drying phase.

Modeling

To establish a physics-based corrosion model, we start the framework of modeling from the atomistic scale first. The development of a magnesium interatomic potential using the Modified Embedded Atom Method (MEAM) to describe accurately dislocation properties is presented. The goal is to compare different atomic potentials for Mg based on the relaxed $\langle 10\bar{1}0 \rangle$ -generalized stacking fault (GSF) energy curve and the Peierls stress of an edge dislocation lying in the basal plane and then develop a new potential that satisfies both more appropriately.

Van Swygenhoven and coworkers (2004) claimed that the nature of slip in nanocrystalline metals cannot be described in terms of an absolute value of the stacking fault energy, but a correct interpretation requires the GSF energy curve to include both the stable and unstable stacking fault energies. In this way, a simple measure for the relative tendency of a material to nucleate full dislocations is given by the ratio of the unstable to stable stacking fault energy. If this ratio is close to unity, it will be easier for full dislocations to be nucleated, and if it is high, it will be more difficult and mostly extended stacking faults from single partial dislocations will be observed in Molecular Dynamics (MD) simulations. Unfortunately, the unstable stacking fault energy is not experimentally accessible, and the stable stacking fault energy values are reported with large scatter in magnesium, ranging from 60 mJ/m² up to 150 mJ/m² based on the experimental data and between 29 mJ/m² and 47 mJ/m² using first principles methods. In addition, although experiments do not give access to the complete GSF energy curve, first principle calculations can be used as an input for the development of an interatomic potential.

The Embedded-Atom Method (EAM) and Modified Embedded-Atom Method (MEAM) potentials are based on molecular dynamics principles. The total energy of an atomic system, E , is calculated by summing the individual embedding energy F_i of each atom, i , in the atomic aggregate, as follows:

$$E = \sum_i E_i = F_i \left(\sum_{j \neq i} \rho_i(r_{ij}) \right) + \frac{1}{2} \quad (1)$$

where, j is any neighboring atom, r_{ij} and Φ_{ij} are the mean separation and pair potential, respectively, between atoms i and j . The EAM models used for this work were those of Liu et al. (1996) and Sun et al. (2006). These two EAM models are essentially identical, with the exception of the form of the embedding energy function employed; In Liu et al., the embedding energy was represented by a general function that needed to be determined, while in Sun et al., the embedding energy function was represented by a square root. The MEAM models studied in this effort were those of Baskes and Johnson (1994) and a new set of MEAM parameters developed to model dislocations more accurate during this study. Compared to the EAM potentials, the MEAM models present the advantage of taking into account the angular dependence of bonding. The coefficients of these potentials were chosen to fit material properties such as the lattice parameter, cohesive energy, unrelaxed vacancy formation energy, elastic constants, crystal lattice, and liquid and melting properties.

Using the Mg database given in Table 1, a new set of parameters to model magnesium using the MEAM formalism was determined. The lattice parameters, elastic constants, energy of both the fcc and bcc phases, and the vacancy formation energy obtained with the MEAM parameters given in Table 2 are reported in Table 1. Relatively good agreement between the target value and the value calculated using the MEAM parameters was obtained except for the energy of the fcc phase.

Table 1. Mg database for the development of a MEAM potential.

Properties	Units	Target value	New MEAM potential
a	Å	3.203	3.202
c/a	-	$0.994 \times (8/3)^{0.5}$	$0.99 \times (8/3)^{0.5}$
$E_{\text{coh}} = E_{\text{hcp}}$	eV	1.51	1.51
E	GPa	35.2	35.2
c_{11}	GPa	59.3	57.7
c_{33}	GPa	61.6	60.0
c_{44}	GPa	16.4	16.3
$c_{11} - c_{12}$	GPa	16.8	16.8
E_{bcc}	eV	0.031	0.025
E_{fcc}	eV	0.026	0.008
E_{vac}	eV	0.40	0.35

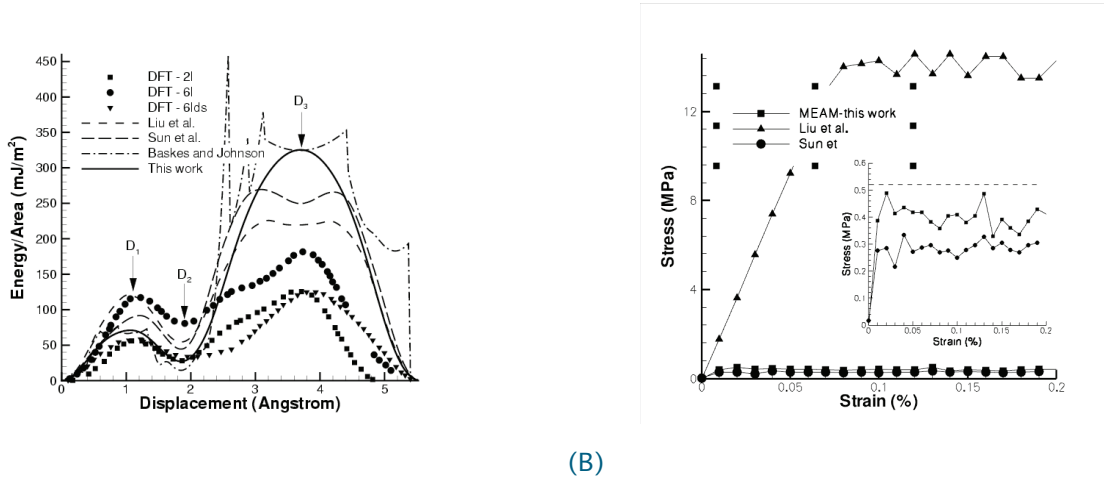
Table 2. Mg MEAM coefficients.

A	α	β_0	β_1	β_2	β_3	r_c (Å)	E_c (eV)	t_0	t_1	t_2	t_3	C_{min}	C_{max}
0.7	5.49	4.6	0.2	0.4	0.8	3.19	1.51	1	4.64	19.97	-6.52	0.5	2.8

Using a lattice of small dimensions, the $\langle 10\bar{1}0 \rangle$ -GSF energy curves calculated using either the Liu et al., Sun et al. and Baskes and Johnson potentials are plotted in Figure 3.1A and compared with the first principle results reported by Datta et al. (2008). Although the Baskes and Johnson MEAM potential was able to reproduce the physical properties reported in Table 1, its application for dislocation purposes was compromised by the discontinuity in slope of the GSF energy curve due to the neglect of second nearest neighbor interactions. On the other hand, calculations performed with the Sun et al. and Liu et al. potentials exhibited behavior similar to

the DFT results until the intrinsic stacking fault was formed (label D_2 in Figure 4(A)); then fairly large deviations were experienced. For a displacement larger than 2 \AA , the EAM models did not reproduce both the shape and the magnitude of the GSF obtained by Datta and coworkers.

To remove the discontinuity in slope of the GSF energy curve obtained with the Baskes and Johnson MEAM potential, a decrease of the screening parameter (C_{\min}) from 2.0 to 0.5 was required. This change introduced second nearest neighbor bonds. Such a change of the screening functions affected all the physical properties reported in Table 1. Therefore, the other parameters of the MEAM potential needed to be adjusted accordingly. The $\langle 10\bar{1}0 \rangle$ -GSF energy curve calculated using the improved MEAM potential is shown in Figure 4(A).



(A) (B)
Figure 4: Generalized stacking fault energy curves (A) and Strain-stress curves obtained crystals oriented for basal slip (B) calculated with different interatomic potentials.

Until the intrinsic stacking fault was formed, the MEAM prediction followed the lower bound given by Datta et al. (2008). Although a maximum energy was reproduced for a displacement of 3.7 \AA , the magnitude of the energy was out of the range given by Datta et al. The magnitude of the second maximum was strongly affected by the difference of energy between the simple cubic and hexagonal crystal structure. However, such a difference of energy was not taken into account in the material database, and therefore, the second maximum was not adjusted for the fitting. No size effect was observed when a lattice of large dimensions was considered for the calculations of the GSF-energy curves.

As a benchmark of the improved potential, the dislocation core structure of the edge dislocation lying in the basal plane, and its Peierls value were tested. Dislocations were introduced in the crystal following the methodology given by Groh et al. (2009). Except for the Baskes and Johnson MEAM potential that could not be used to minimize the dislocation structure because of the discontinuities in the slope, edge dislocations from the basal plane were dissociated into two Shockley partials bounding an intrinsic stacking fault of length d_{sf} . The separation distance is given as a function of the Poisson coefficient, intrinsic stacking fault energy, and Burgers vector using the isotropic elasticity (IET) (Hirth and Lothe (1992)). Using the anisotropic elasticity theory (AET), the separation distance is given by

$$d_{sf}^{aniso} = \frac{b^2}{32\pi\gamma_I} \left[4K_e - \frac{K_s}{3} \right]$$

with

$$K_s = (c'_{44}c'_{55})^{1/2}; \quad K_e = \left(\frac{c_{11}c_{22} - c_{12}^2}{c_{11} + c_{22}} \right)^{1/2}$$

where the elastic constants are given by

$$c'_{11} = c_{11}; c'_{12} = c_{13}; c'_{44} = c_{44}; c'_{66} = c_{66}; c'_{22} = c_{33}; c'_{11} = (c'_{11}c'_{22})^{1/2}$$

For the elastic constants obtained with both Liu et al. and the improved MEAM potential, the elasticity framework (isotropic versus anisotropic) did not significantly affect the separation distance. On the other hand, as the elastic constants were sacrificed by Sun et al. to accurately reproduce the thermal properties of Mg, the elasticity framework (isotropic versus anisotropic) strongly affected the prediction of separation distance (see Table 3).

Table 3. Evolution of the separation distance between partial dislocations using different interatomic potentials and comparison with isotropic/anisotropic elasticity theory for different cell size (in Burgers vector, b).

	Separation distance (nm)		
	Liu et al.	Sun et al.	This work
IET	1.56	1.28	2.58
AET (Eq. 2)	1.90	2.22	2.87
Cell dimension (b*b)			
30x30	1.24	1.76	2.52
100x100	1.53	2.17	2.66
200x200	1.54	2.16	2.80
300x300	1.53	2.16	2.81

Independent of the potential considered, the atomistic predictions of separation distance were size independent for a cell size bigger than 100bx100b (where b is the magnitude of the Burgers vector) as shown in Table 3. Based on the flexible *ab-initio* boundary condition method, Yasi et al. (2009) calculated the dislocation core structure of an edge dislocation lying in the basal plane using a cylinder of radius 22b. Their results confirmed the dissociation in two partials with a separation distance of 1.67 nm. Compared to their results, only the prediction obtained with the Sun et al. potential and a computational box of small dimension agreed with that value, while predictions were underestimated and overestimated using the Liu et al. and the MEAM potentials, respectively. Such a difference can be attributed to the value of the intrinsic stacking fault energy. In our case, the potential was fit based on the data reported by Datta et al. (2008) which represents a lower bound, while the intrinsic stacking fault obtained with the Liu et al. potential represents an upper bound.

Figure 4(B) shows the strain-stress behaviors calculated with the three different potentials and using a simulation cell of dimension 200bx200b along the line and displacement directions oriented to model the motion of an edge dislocation lying in the basal slip plane with a strain increment of 10^{-4} . As shown in Groh et al. (2009), no significant effect of the strain increment was found. Using the Liu et al. potential, the stress increased linearly up to 15 MPa before it stabilized. The corresponding shear modulus was 18.7 GPa, which is in good agreement with the value reported by Liu et al. ($C_{44} = 18.1$ GPa). So, for this potential, the Peierls stress was close to 15 MPa, a value one order of magnitude larger than the experimental value reported by Conrad and Robertson (1957). On the other hand, both the MEAM and Sun et al. potentials gave a Peierls stress in the order of 0.3-0.5 MPa, which is in closer agreement with the experimental data.

Conclusions

The corrosion test results showed that the most corrosive test cycle was the Salt Spray-Humidity-Drying cycle. The cyclical corrosion testing demonstrated that chloride ions were necessary to initiate pitting, humidity was necessary to initiate galvanic corrosion between the eutectic and grain phases as well as necessary to provide hydrogen ions for further corrosion, and drying was necessary to trap water and chloride ions beneath the corrosion by-products, allowing the pits to grow rapidly before the dominant corrosion mechanism switched to general

corrosion. The immersion/salt spray longitudinal study showed that immersion allowed for the formation of more pits that were larger in size and closer together than the salt spray coupons. The continuous presence of water in the immersion cycle meant that general corrosion could occur alongside pitting and intergranular corrosion, removing corrosion debris and allowing the pits to continue to grow.

Bridging different length scales for the analyses of plasticity, damage, fracture/fatigue, and alloying, we have to establish atomistic simulations of materials. Optimizing the MEAM potential to the generalized stacking fault (GSF) energy curve and the Peierls stress is necessary to capture the appropriate dislocation behavior, as the standard procedure of using just the elastic modulus and cohesive energy is not robust enough. The improved magnesium MEAM model was correlated with both experimental and ab initio results. The improved magnesium MEAM model accurately predicted physical properties, such as lattice parameter, the vacancy formation energy, and the GSF energy curves for basal slip, as well as mechanical properties, such as elastic constants and Peierls stress for basal slip.

The experimentation by-products of the corrosion of magnesium include hydrogen atoms; those atoms form hydrochloric acid, hydrogen gas, and hydrogen ions. The hydrogen ions have the capability to diffuse into the magnesium, eventually resulting in the embrittlement of the magnesium metal. The dislocation modeling will include the effect of hydrogen on the dislocations within the magnesium metal. By combining the information provided by the experimental corrosion tests and dislocation modeling methods, the effects of voids caused by pitting and the effects of hydrogen produced by corrosion on the dislocations and voids within the magnesium will be elucidated in our near future efforts.

Publications

1. Groh S, Horstemeyer MF, Baskes MI. (2009). Dislocation nucleation related to the peierls stress and generalized stacking faults in magnesium using embedded atom method and modified embedded atom method potentials in molecular statics, Scripta Mat. In review; submitted.
2. Groh S, Marin EB, Horstemeyer MF. (2009) Nanoscale void growth in magnesium: A molecular dynamics study, Int J Appl Mech. In Press; accepted.
3. Groh S, Zbib HM. (2009). Advances in discrete dislocations dynamics and multiscale modeling. J Eng Mat. Tech 13:041209-1-10.
4. Martin HJ, Horstemeyer MF, Wang PT. (2010). Effects of salt-spray, humidity, and drying on an as-cast AE44 magnesium alloy, Int J Corro. 2010, 1-10, doi: 10.1155/2010/602342.
5. Alvarez RB, Martin HJ, Horstemeyer MF, Chandler MQ, Williams N, Wang PT, and Ruiz A. (2010). Structure-property corrosion relationships of a structural AE44 magnesium alloy. Corros Sci. 52, 1635-1648.
6. Martin HJ, Alvarez RB, Horstemeyer MF, Chandler MQ, Williams N, and Wang PT. (2009). Corrosion relationships as a function of time on a structural AM60 magnesium alloys, Corros. NACE. In review; submitted.

Presentations

1. Groh S, Marin EB, Horstemeyer MF, and Zbib HM. (2009). Multiscale modeling of the plasticity in an aluminum single crystal, USNCCM09; Columbus, OH; 2009 July.
2. Martin HJ, Horstemeyer MF, Wang PT. (2009). Corrosion mechanisms occurring on AE44 Mg exposed to a 3.5% NaCl Aqueous Solution: Experimental effects. American Institute of Chemical Engineers Annual Meeting; Nashville, TN; 2009 November.
3. Martin HJ, Horstemeyer MF, Wang PT. (2009). Corrosion mechanisms occurring on AM60 Mg exposed to a 3.5% NaCl Aqueous Solution: Experimental effects. American Institute of Chemical Engineers Annual Meeting; Nashville, TN; 2009 November.
4. Martin HJ, Horstemeyer MF, Wang PT. (2009). Pit nucleation, growth, and coalescence: Modeling the corrosive effects of Mg exposed to a 3.5% NaCl aqueous solution. American Institute of Chemical Engineers Annual Meeting; Nashville, TN; 2009 November.

References

1. Alvarez RB, Martin HJ, Horstemeyer MF, Chandler MQ, Williams TN, Wang PT, Ruiz A. (2010). Structure-property corrosion relationships of a structural AE44 magnesium alloy. *Corros. Sci.* 52, 1635-1648.
2. Bakke P, Westengen H. (2005). The role of rare elements in structure and property control of magnesium die casting alloy. In N.R. Neelameggham, H.I. Kaplan, B.R. Powell (Eds.), *TMS – Magnesium Technology*. 291-296.
3. Baskes MI, Johnson RA. (1994). Modified embedded atom potential for HCP metals. *Modelling Simul. Mater. Sci. Eng.* 2, 147-63.
4. Conrad H, Robertson WD. (1957). Effect of temperature on the flow stress and strain hardening coefficient of magnesium single crystal. *TMS-AIME*. 209, 503-12.
5. Datta A, Waghmare UV, Ramamurty U. (2008). Structure and stacking faults in layered Mg-Zn-Y alloys: A first-principles study. *Acta Mater.* 56, 2531-39.
6. Fontana MG. (1986). Corrosion Principles, in: M.G. Fontana (Eds.), *Corrosion Engineering*, McGraw-Hill, Boston. 12-38.
7. Groh S, Marin EB, Horstemeyer MF, and Bammann DJ. (2009). Dislocation motion in magnesium: a study by molecular statics and molecular dynamics. *Modelling Simul. Mater. Sci. Eng.* 17, 075009.
8. Hirth JP, Lothe J. 1992. *Theory of dislocations*. Malabar (FL): Krieger Publishing Company.
9. Liu XY, Adams JB, Ercolessi F, and Moriarty JA. (1996). EAM potential for magnesium from quantum mechanical forces. *Modelling Simul. Mater. Sci. Eng.* 4, 293-303.
10. Makar GL, Kruger J. (1993) Corrosion of magnesium. *Int. Mater. Rev.* 38, 138-153.
11. Shaw BA. (2003). Corrosion Resistance of Magnesium Alloys, in: L.J. Korb, ASM (Eds.), and ASM Handbook, Vol. 13A: Corrosion, Ninth Ed., ASM International Handbook Committee, Metals Park. 692.

12. Song G, Atrens A. (2003). Understanding magnesium corrosion – a framework for improved alloy performance, *Adv. Eng. Mater.* 5, 837-858.
13. Sun DY, Mendeleev MI, Becker CA, et al. (2006). Crystal-melt interfacial free energies in hcp metals: A molecular dynamics study of Mg. *Phys Rev B* 73, 024116.
14. Swygenhoven HV, Derlet PM, Frøseth AG. (2004). Stacking fault energies and slip in nanocrystalline metals. *Nature Mat.* 3, 399-403.
15. Yasi JA, Nogaret T, Trinkle DR, Qi Y, Hector LG and Curtin, WA. (2009). Basal and prism dislocation cores in magnesium: comparison of first-principles and embedded-atom-potential methods predictions. *Modelling Simul. Mater. Sci. Eng.* 17, 055012

G. Nano-Engineered Cast Components (NECC) Phase I: Elevated Temperature Mechanical Property Testing and Cost Model Development

Principal Investigator: Xiaochun Li
Jasmade Innovations LLC
8421 Castle Pines Drive
Madison, WI 53717
(608)833-8146; e-mail: aiping_ca@yahoo.com

Technology Area Development Manager: William Joost
(202) 287-6020; e-mail: william.joost@ee.doe.gov

Field Project Officer: Magda A. Rivera
(304) 285-1359; email: magda.rivera@netl.doe.gov

Expert Technical Monitor: C. David Warren
(865) 574-9693; e-mail: warrencd@ornl.gov

Participants:

Mark Osborne, General Motors Corp.; mark.osborne@gm.com (project leader)
Bob Powell, General Motors Corp.; bob.r.powell@gm.com
Jake Zindel, Ford Motor Co.; jzindel@ford.com

Contractor: United States Automotive Materials Partnership (USAMP)
Contract No.: DE-FC05-02OR22910 through the National Energy Technology Laboratory

Objective

- Demonstrate enhanced thermo-mechanical properties of nanoengineered aluminum-matrix composite alloys for future powertrain applications
- Develop cost model to assess the cost effectiveness of nanoengineering aluminum-matrix composite alloys

Approach

- Prepare nanocomposites using ultrasonic cavitation methods to disperse nanoparticles in molten aluminum A356 and cast specimens for analysis
- Evaluate nanocomposite fatigue and tensile properties
- Create a cost model for nanocomposite manufacture to determine its cost effectiveness

Accomplishments

- Set up an ultrasonic processing unit with an improved powder feeding method for dispersing nanoparticles in molten aluminum A356
- Explored a pretreatment method for nanoparticle surface preparation

- Completed initial casting trials of A356 and A356-matrix nanocomposites for specimens for mechanical testing
- Characterized the microstructures of nanoparticles and nanostructured castings

Future Direction

Research completed. Will consider future work as appropriate.

Introduction

Aluminum alloys (Al) have great potential for improving the energy efficiency of transportation systems. However, their mechanical properties, especially their property degradation at elevated temperatures, present a potential roadblock to their wider use in the demanding environments of advanced powertrain applications. The properties of Al alloys can be enhanced considerably if nanoparticles are used as a reinforcement to form nano-structured Al materials. A fine and uniform dispersion of nanoparticles provides a good balance between the strengthener (non-deforming particles, such as inorganic nanoparticles) and inter-particle spacing effects to maximize the yield strength and creep resistance (by mechanisms such as dislocation bowing around the particles and pinning down dislocations at the particles by rapid diffusional stress relaxation at elevated temperatures) while retaining the good matrix ductility [1-4]. It is proposed that a fine, uniform dispersion of nanoparticles can provide dispersion strengthening (as non-deforming particles, such as inorganic nanoparticles). They may also provide inter-particle spacing effects such as increasing the yield strength and creep resistance by mechanisms such as dislocation bowing around the particles and the pinning of dislocations at the particles by rapid diffusional stress relaxation at elevated temperatures. These benefits require only a small percentage of nanoparticles (less than 2%) in the casting. Nevertheless, the main limitation to wider use of nanoparticle reinforcement is the cost of the nanoparticles and of their processing (dispersion) into metal melts. It is anticipated that with increasing mass production, the cost of nanoparticles will become significantly lower, which could make the production of nano-structured Al and Mg cost effective.

The current processing methods for bulk nanostructured Al materials are limited in size and geometric complexity, preventing designers from achieving the design flexibility desired for complex automotive and aerospace structures. The potential of nano-structured Al materials cannot be fully developed for industrial applications unless complex structural components of the nano-structured Al materials can be fabricated cost effectively, such as by casting. Nor can reliable nano-structured Al parts be cast unless nanoparticles can be dispersed and distributed uniformly in molten Al. Unfortunately, it is extremely challenging for conventional mechanical stirring methods to distribute and disperse nanoparticles uniformly in metal melts due to the large surface-to-volume ratio of the particles, and their poor wettability in most liquid metals which results in agglomeration and clustering. Thus, there is a strong need for a cost effective and reliable process that enables efficient and stable dispersion of nanoparticles in Al melts for casting of high performance nano-structured Al materials.

Our preliminary experiments demonstrate that ultrasonic cavitation is effective in dispersing and stabilizing ceramic nanoparticles in aluminum alloy melts for casting in small crucibles. Substantial basic research and development must be performed to establish an engineering science and technology base for a solid understanding of strengthening, deformation, creep, and fatigue mechanisms in the nanometer range. This NECC project Phase I was aimed at measuring the elevated temperature tensile properties and fatigue properties of the A356 alloy nanocomposite and developing a cost model structure for fabricating this material.

Results and Discussion

Task 1. CASTING AND MECHANICAL TEST OF A356 NANOCOMPOSITES

1.1 Developed an efficient nanoparticle feeding method

The usual method for blending nanoparticles into molten metal is by manual “ladling” and stirring. This process is time consuming and prone to introducing defects/inclusions as a result of poor dispersion of the nanoparticle aggregates. Ultrasonic excitation has been shown to reduce dispersion time and to improve the degree of dispersion [4-6]. In the present work, a commercially available ultrasonic transducer with acoustic energy (up to 600W) and frequency of approximately 20 KHz was used. The acoustic transducer transfers vibrations into metal melts via a niobium waveguide, which can withstand temperatures as high as 1200°C for 300 hours with minimum ultrasonic erosion. This energy is sufficient to break up the SiC aggregates. The Task 1.1 goal was to develop methods for placing the SiC nanoparticles below the A356 melt surface close to the tip of the ultrasonic probe so that dispersion would be maximized. The approach taken was to roll the nanoparticle SiC powder into Al foil and to roll the foil into the shape of long rods. The rods were then pushed into the melt near the ultrasonic tip. As the Al melted and released the SiC, the rod was lowered further into the melt. This was shown to be more effective than manual ladling and stirring. With the new nanoparticle feeding method, the time for feeding and dispersion reduced from 45 minutes to about 5 minutes.

1.2. Conduct mold design and casting experiments

The objectives of this task were to produce defect-free tensile bars and to minimize the amount of A356 nanocomposite needed for mechanical testing. A low carbon steel mold was designed and fabricated according to ASTM B108-03a for casting standard round tensile specimens with a diameter of 9.5 mm and a gage length of 44.5 mm as shown in Figure 1 (a). A silicon carbide ceramic foam filter with a dimension of 55 mm × 55 mm × 12 mm and a pore size of 20 ppi (pores per inch) was used to remove inclusions. A second low carbon steel mold was also evaluated. This mold was provided by Beck Foundry Supply (Missouri, USA), as shown in Figure 1b. It produced larger standard round tensile specimens with a diameter of 12.7 mm and a gage length of 50.8 mm. For this mold, the ceramic foam filter with the dimension of 38.1 mm × 38.1 mm × 12.7 mm and the pore size of 15 ppi was placed inside the mold. It was expected that this mold would produce higher quality specimens by reducing the degree of melt oxidation during pouring. The filter (white) can be seen at the bottom of the down sprue in Figure 1 (b).

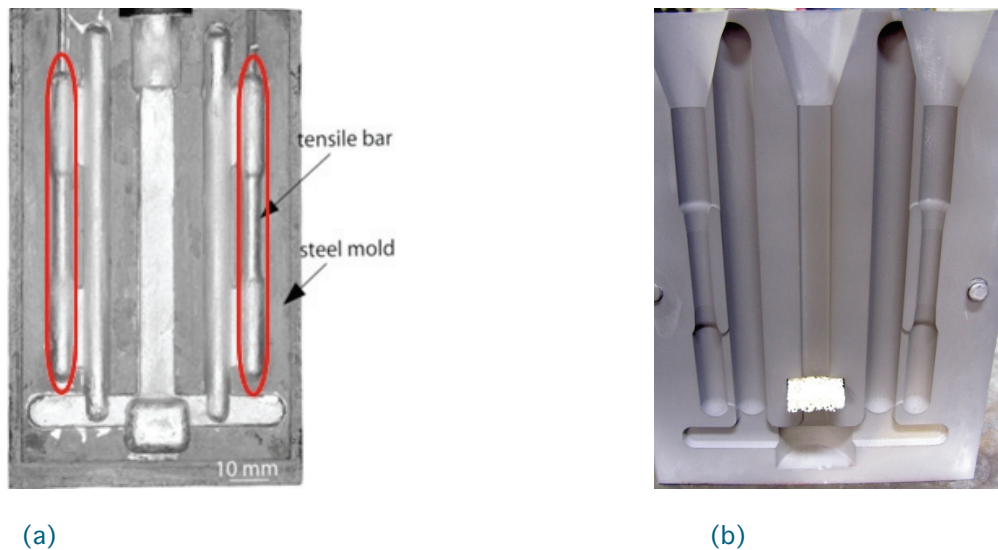


Figure 1. Low carbon steel molds



Figure 2. Cast of A356 aluminum alloy with larger mold

However, casting trials with this mold were plagued with incomplete filling. Figure 2 shows that the incomplete fill produced tensile specimens with short upper grips.

Both of the above molds used too much metal. In order to save the amount of molten metal for each casting and to increase the number of process cycle, another mold with smaller dimension was designed and fabricated according to ASTM B108-03a, as shown in Figure 3. Low carbon steel pouring cup, which was coated with boron nitride thin layer, was used to guide the melt and serve as housing for the steel mesh with a mesh size of 24×24 . The interaction time between the mesh and molten A356 is very short and there was no concern of Fe contamination.

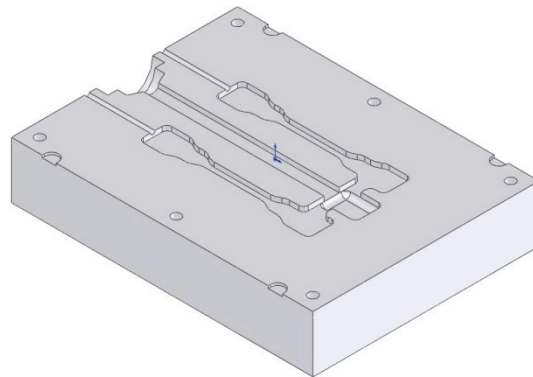


Figure 3. Final mold design with improved casting yield

1.3. Create a processing procedure to ensure a more consistent casting

A procedure was developed for processing the alloy from ingot and for casting test specimens. It is described below.

1.4. Casting of A356 and its nanocomposite tensile specimens

A356 was melted and cast after superheating to 700°C . SiC-reinforced A356 (1.0 volume percent 25 nm SiC nanoparticles) was also superheated to 700°C and then processed with optimized ultrasonic excitation conditions (vibration amplitude). Casting was done under argon protection. After ultrasonic processing, the melts were cast into the molds. The melt pour temperature was 740°C . The resulting cast specimens were tensile tested.

1.5. Analysis of A356 tensile testing results

Tensile testing was done with the specimens produced from the small mold. The tensile specimens with a dimension of 6.35 mm × 6.35 mm and a gage length of 38.1 mm were obtained. They were tested on a Sintech 10/GL. The pure A356 samples (as-cast) test results were ~79 MPa and ~159 MPa for yield and ultimate tensile strength, respectively. The elongation was about 3%.

The yield strength results of the cast aluminum nanocomposites showed a fluctuating enhancement from 35% to 60%, i.e. yield strength fluctuating from 102MPa to 128MPa, in as-cast form. The elongation is generally ~0.5% better than that of pure cast A356, while the tensile strength results showed a 25% to 45% enhancement.

Task 2. MICROSTRUCTURAL CHARACTERIZATION

2.1. SEM Analysis of nanoparticle dispersion

Samples of the cast composites were cut and mounted with epoxy, and mechanically polished down to 0.05 μ m surface finish. SEM images were obtained with a LEO1530 scanning electron microscope. While not all SiC nanoparticles were dispersed uniformly, some dispersion was achieved, as shown in [Figure 4](#).

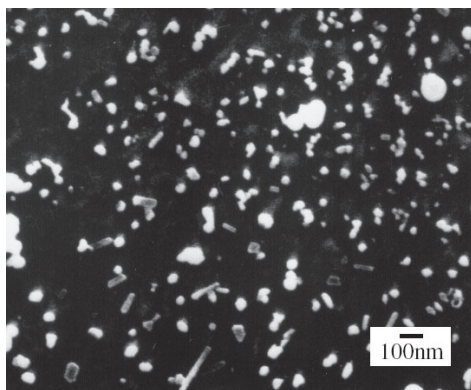


Figure 4. Nanoparticle dispersion in A356

2.2. Nanoparticle characterization and understanding

When several packages of SiC nanopowders were ordered for metal-matrix nanocomposite processing and casting, it was observed that each package of the nanopowders, of the same radius, exhibited different features such as density and color. The inconsistency of the tensile data reported above was attributed to these powder differences. Powder differences considered included the degree of SiC oxidation and the presence of impurities. The phase composition of each SiC package was characterized through X-ray diffraction (XRD). Two particular SiC packages were investigated, SiC-B, which is a dark gray powder, 20-30 nm in size, from NanoAmor Inc., and SiC-II, which is a black powder, also 20-30 nm in size, from NanoAmor Inc. XRD analysis was conducted using a Scintag PADV X-ray diffractometer. The 2 θ scan range was 20-90 degrees with a 0.02 degree scan rate and a 1.0 sec dwell time.

Analysis of the SiC-B spectra determined that the sample consisted mostly of the hexagonal-structured SiC, or α -SiC. In contrast, analysis of the SiC-II spectra determined that the sample consisted mostly of the cubic-structured SiC or β -SiC. Therefore, from this analysis, it is concluded that the structure of each SiC package must be investigated before processing and casting to determine its relation to MMNC performance.

A procedure for particle quality control was developed, which specified such powder attributes as purity, average particle size (APS), specific surface area (SSA), color, morphology, bulk density, true density and crystallographic system. This set of specifications will form the basis for future work in this area.

Conclusion

Nanoparticle reinforcement of aluminum alloy showed good enhancement over their pure alloy while retaining ductility. But the enhancement was still less than the better enhancement data reported in literature [6]. Experimental problems and inconsistencies in nanoparticle quality from market, materials and handling are to some extent responsible for the results. Testing trials with two different nanoparticle sources revealed significant variations in chemistry, color (indicative of oxidation and impurities), and crystallinity (cubic vs. hexagonal). It is believed that these differences significantly affected the tensile properties, but further investigation is needed. A characterization procedure was developed to analyze the incoming nano-powder material. This should provide the basis for generating a specification for nanoparticles from market. A processing procedure for the manufacture of the nano-aluminum material was developed. While following this procedure should improve the consistency of experimental results, this remains to be validated by experiments.

References

1. T.H. Courtney, Mechanical Behavior of Materials (McGraw Hill, 2001)
2. R.J. Arsenault, L. Wang, and C.R. Feng, *Acta Metal. Mater.*, **39** (1), 47 (1991)
3. N. Ramakrishnan, *Acta Mater.*, **44**, 69 (1996)
4. Y. Yang, J. Lan and X.C. Li, *Materials Science and Engineering A*, **380**, 378 (2004)
5. Suslick, K.S. (ed.), *Ultrasound: Its Chemical, Physical, and Biological Effects* (VCH, New York, 1988)
6. X.C. Li, Y. Yang, and D. Weiss, *AFS Transaction*, #07, 135 (2007)